minerals

MDPI

Article

Fracture Development in Alkaline Lacustrine Shales: Insights from Multi-Stage Fluid–Rock Interactions in the Permian Fengcheng Formation, Mahu Sag, Junggar Basin

Kuan Lu [1], Jiakai Hou [2], Zhenkai Huang [3,4], Guangyou Zhu [1,*], Jianyong Liu [1], Jiangna Fu [3,4] and Heting Gao [1]

[1] Hubei Key Laboratory of Complex Shale Oil and Gas Geology and Development in Southern China, Yangtze University, Wuhan 430100, China; geolukaun@163.com (K.L.); 2021710491@yangtzeu.edu.cn (H.G.)
[2] Research Institute of Petroleum Exploration and Development, PetroChina, Beijing 100083, China
[3] State Key Laboratory of Shale Oil and Gas Enrichment Mechanisms and Effective Development, Beijing 102200, China
[4] Sinopec Petroleum Exploration and Production Research Institute, Beijing 102200, China
* Correspondence: zhuguangyou@yangtzeu.edu.cn

Abstract

The Mahu Sag, a hydrocarbon-rich depression within the Junggar Basin, hosts significant petroleum resources. Here, the Permian Fengcheng Formation shale oil reservoirs have emerged as a primary exploration target. This study investigates fracture development within these alkaline lacustrine shales, a critical factor governing hydrocarbon migration and accumulation. Through integrated petrographic and geochemical analyses, we elucidate a multifactorial fracture formation mechanism driven by the interplay of alkaline minerals, stress, and fluids. Two distinct fracture types were identified: bedding-complex fracture veins (BCFVs) and Y-shaped high-angle fracture veins (Y-HFVs). Both fracture types result from alkaline fluid–rock interactions, which induce fracture opening along specific orientations, alter fracture angles, and control aperture width and final morphology. Alkaline mineral assemblages further influence fracture evolution via dissolution–precipitation cycles. Concurrently, these assemblages preserve hydrocarbons by inhibiting the thermal maturation of organic matter, as evidenced by variations in fluid inclusion fluorescence. The fracture networks act as crucial migration pathways, with the BCFV containing higher-maturity hydrocarbons (indicated by blue-green fluorescence) and the Y-HFV retaining less mature fluids (indicated by yellow-green fluorescence). This study presents the first systematic characterization of the multifactorial controls on fractures in alkaline lake environments, proposing a cooperative "alkaline minerals–stress–fluids" mechanism. These findings provide a new framework for understanding fracture development in alkaline lacustrine shales and offer valuable insights for shale oil exploration in analogous depositional settings.

Keywords: alkaline lacustrine shale; fracture genesis; hydrocarbon evolution; Fengcheng Formation; Mahu Sag

Check for updates

Academic Editors: Fabio Trippetta and Shu Tao

Received: 25 March 2026
Revised: 17 April 2026
Accepted: 18 April 2026
Published: 21 April 2026

Copyright: © 2026 by the authors. Licensee MDPI, Basel, Switzerland. This article is an open access article distributed under the terms and conditions of the Creative Commons Attribution (CC BY) license.

1. Introduction

Shale oil has become a cornerstone of unconventional hydrocarbon exploration and is integral to the global energy portfolio [1,2]. The successful exploitation of these resources hinges on a sophisticated understanding of the geological controls governing reservoir quality, particularly the pervasive influence of fluid–rock interactions [3,4]. These interactions

are a key process controlling reservoir formation, evolution, and hydrocarbon enrichment [5]. They not only affect the pore structure and permeability of reservoirs but also determine the openness of fractures and the effectiveness of fluid migration pathways [6,7]. In carbonate and clastic reservoirs, dissolution, precipitation, and metasomatism between different types of fluids and rock minerals can significantly change reservoir physical properties [8,9]. For shale oil and gas reservoirs, the development degree and effectiveness of natural fractures directly affect hydraulic fracturing results and ultimate recovery, while fluid activities in fractures can block pores through mineral precipitation or improve reservoir performance through dissolution [10]. Therefore, in-depth study of rock–fluid interaction mechanisms in shale reservoirs has important theoretical and practical significance for optimizing drilling processes [11] and improving oil and gas exploration and development efficiency [12]. In shale systems, the interplay between diagenetic fluids, host rock mineralogy, and tectonic stress sculpts the reservoir architecture, with natural fractures serving as the primary conduits for fluid flow, enhancing permeability by orders of magnitude over the rock matrix [13]. Mineral veins that seal or partially fill these fractures are direct precipitates from these fluids, encoding a rich history of thermal, pressure, and chemical changes within the basin, thereby offering invaluable insights into fluid–rock reaction dynamics and their impact on hydrocarbon accumulation and preservation [14].

Although extensive research has characterized fracture systems in conventional marine shales, exemplified by multi-stage vein fillings in the Wufeng–Longmaxi Formation [15], our understanding remains limited regarding shales formed in saline, alkaline lacustrine environments, with notable knowledge gaps still existing. The Permian Fengcheng Formation in the Mahu Sag, Junggar Basin, represents a globally unique and challenging frontier in this context [16]. As the world's first confirmed large-scale petroleum system sourced from alkaline lacustrine shales [17], its depositional environment fostered the precipitation of an unusual suite of alkaline minerals (e.g., analcime, reedmergnerite, shortite). This distinct mineralogy, a product of basin salinization and alkaline water chemistry during the Late Paleozoic [18], creates a geochemical playground for fluid–rock interactions that profoundly diverges from typical clastic or carbonate-rich systems. The intricate coupling of this unique authigenic mineralogy with a complex tectonic and burial history has produced a highly heterogeneous fracture network whose development and role in hydrocarbon enrichment remain poorly constrained.

Previous studies on the Fengcheng Formation have successfully characterized its complex lithofacies and confirmed the presence of diverse natural fracture systems, including both bedding-parallel and high-angle fractures, acknowledging their general importance for reservoir quality [19,20]. However, most of these studies have focused on the macroscopic characteristics of fracture networks, while paying insufficient attention to the ore-forming minerals within fracture veins and their evolutionary history with fluids. The existing literature rarely touches upon the microscopic genesis mechanism of fracture veins. There is a lack of a mechanistic model that explains their multi-stage opening and mineralization within the unique chemo-mechanical environment of alkaline shales. Key unresolved issues include: (1) How does the synergistic interplay of tectonic stress, overpressure from hydrocarbon generation, and the reactive nature of alkaline fluids govern the initiation, propagation, and healing of these fracture veins? (2) What are the distinct evolutionary pathways of different vein types, and how do their formation histories relate to the timing of hydrocarbon charging? (3) Most importantly, how do the intense, multi-stage fluid–rock interactions involving highly alkaline fluids affect the subsequent thermal evolution and preservation of entrapped hydrocarbons within these fracture networks? The answers to these questions are vital for de-risking exploration and optimizing stimulation strategies in this and other similar alkaline lacustrine basins.

To address these critical knowledge gaps, this study undertakes a comprehensive investigation of fracture veins within the Lower Permian Fengcheng Formation shales in the Mahu Sag. By integrating detailed petrographic observations with advanced geochemical and micro-analytical techniques, we aim to unravel the complex history of fracture development. Our multi-proxy approach utilizes: (1) elemental mapping to delineate the spatial distribution of vein-filling minerals and reconstruct dissolution–precipitation sequences; (2) cathodoluminescence (CL) imaging to distinguish successive cementation phases and decipher the multi-stage growth history of the veins; (3) fluid inclusion thermometry to quantitatively track the paleo-temperature during fracture evolution; and (4) carbon, oxygen, and strontium isotopic analyses to trace the origin, evolution, and redox conditions of diagenetic fluids.

Through this integrated analysis, we deconstruct the formation mechanisms and evolutionary histories of two dominant vein types, revealing their relationship with hydrocarbon charging events. The central objective is to elucidate the dynamic feedback loop between alkaline minerals, stress fields, and migrating fluids, and to assess its ultimate impact on hydrocarbon migration, accumulation, and, most notably, its preservation. This study not only provides a genetic model for fracture development in alkaline lacustrine shales but also reveals a novel mechanism whereby alkaline mineral assemblages actively inhibit the thermal maturation of entrapped oil. These findings offer a new theoretical framework for predicting sweet spots in alkaline shale plays and provide crucial geological insights for the global exploration of unconventional resources in saline lacustrine basins.

2. Geological Settings

The Mahu Sag (Figure 1a,b), situated in the Junggar Basin of Xinjiang, China, is a significant petroleum exploration area within the basin [21]. It is bounded by the Zaire Mountains to the west and the Hala'alate Mountains to the north, contiguous with the Zhongguai Uplift to the south, and adjacent to the Dajingzi and Xiayan Uplifts to the southeast. The sag exhibits a NW-SE trending monoclinal structure with gentle dip angles, locally featuring low-amplitude fault ramp zones. The Mahu Sag developed upon a folded basement formed prior to the Carboniferous period. Influenced by peripheral tectonic activities [22], it underwent a prolonged tectonic evolution spanning the Carboniferous to the Quaternary. This evolution included orogenic events, compressional thrusting, and the development of an intracontinental sag within the craton. Its structural framework comprises the Central Depression, Western Uplift Belt, and the Northern Tianshan Piedmont Slope Zone [23]. The sag is primarily characterized by a fan delta to lacustrine depositional system, with the Permian and Triassic periods representing the main depositional phases [24]. Sediments were sourced from the surrounding uplift zones and mountainous terrains, resulting in the formation of a series of large-scale, shallow-water retrograding fan deltas [25]. Furthermore, the alkaline lacustrine depositional system of the Fengcheng Formation represents another significant characteristic of the Mahu Sag. Its source rocks predominantly comprise organic-rich mudstones and dolomites. Specifically, the Fengcheng Formation source rocks are mainly composed of organic-rich argillaceous limestones and dolomites [22]. These source rocks are in a mature to low-mature evolutionary stage and constitute critical source rocks within the Mahu Sag [18]. The study area is located within the northern slope zone of the Mahu Sag, Junggar Basin. This area is a key exploratory target for investigating both Permian Fengcheng Formation shale oil and conventional volcanic reservoirs. The Fengcheng Formation developed within an alkaline lake environment. Its sedimentary evolution underwent multi-stage evolutionary cycles, including freshwater, salinification, evaporite deposition, and weakly saline phases. This formation exhibits the characteristic

feature of mixed sedimentation, incorporating volcanic material, terrigenous clastics, and carbonates (Figure 1d).

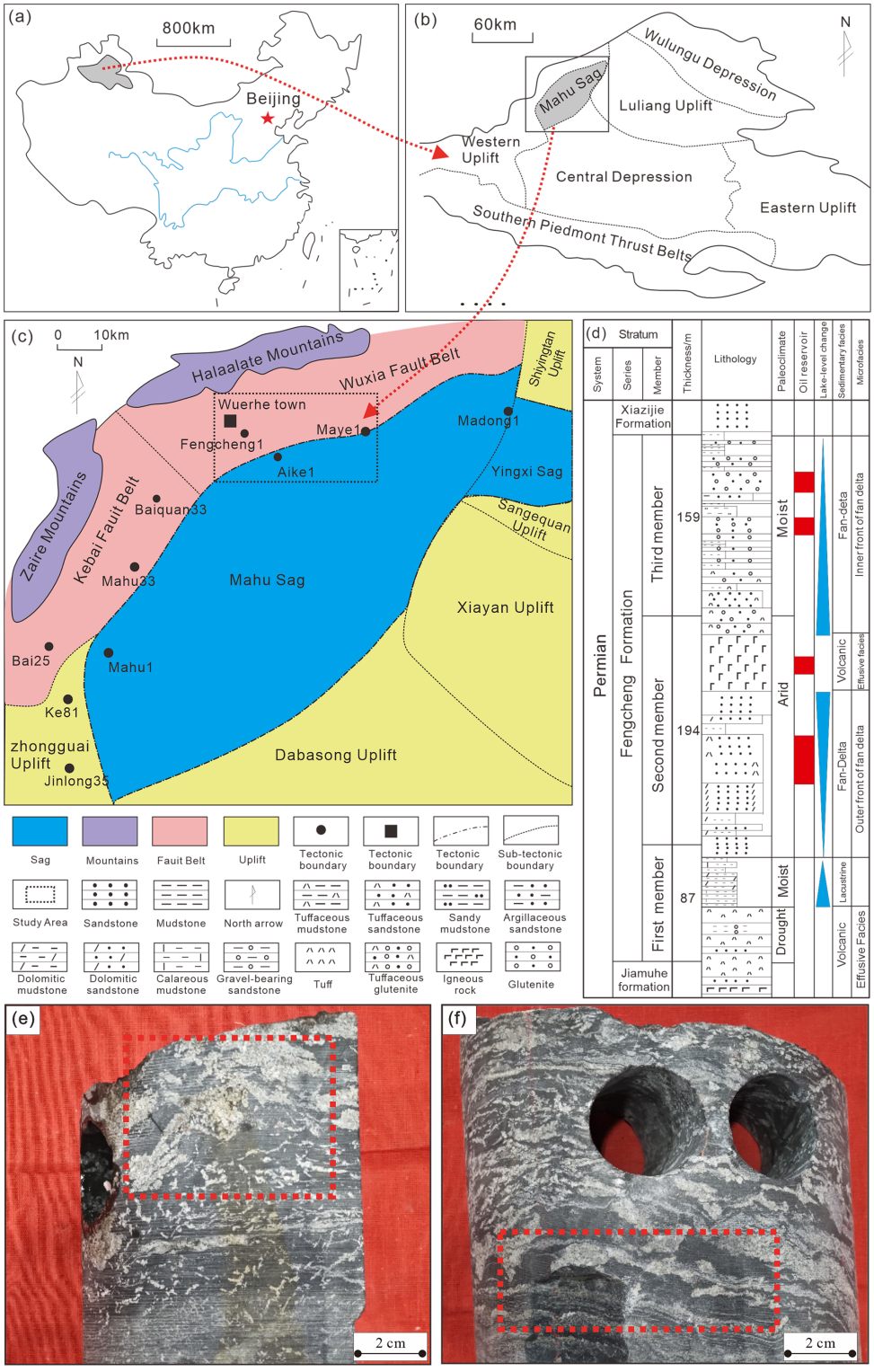


Figure 1. Geological background, sampling well locations, and typical core photos of Mahu Sag, Junggar Basin. (**a**) Location map of China; (**b**) distribution map of tectonic units in Junggar Basin; (**c**) study area and sampling locations; (**d**) integrated stratigraphic column chart of Fengcheng Formation in Mahu Sag; (**e**) typical core sample photos obtained from Fengcheng 1 Well, sampling depth 4273 m; the area circled in red box is Y-shaped high-angle fracture; (**f**) typical core sample photos obtained from Maye 1 Well, sampling depth 4820.17 m; the area circled in red box is bedding-complex fracture veins.

3. Samples and Methods

3.1. Samples

The Maye 1 and Fengcheng 1 Wells, situated within the northern slope zone of the Mahu Sag, Junggar Basin (Figure 1c), are key exploratory wells for investigating both Permian Fengcheng Formation shale oil and conventional volcanic reservoirs [13]. To systematically evaluate the impact of fractures on the enrichment and reservoir characteristics of shale oil, we conducted strict screening and statistical analysis on the core rock samples from two wells. Core observations revealed that bedding-parallel fractures dominate, with associated high-angle fractures (Figure 1e,f). The fracture fillings are primarily composed of carbonate minerals (calcite, dolomite) and siliceous minerals. Core samples of Fengcheng Formation shale were specifically selected from the Permian section. Sampling depths were 4820.17 m (Maye 1 Well) and 4273 m (Fengcheng 1 Well). Samples exhibiting well-developed, complex bedding-parallel fracture veins and high-angle fractures were selected and processed into doubly polished thin sections 80 μm thick.

3.2. Elemental Mapping Analysis

Elemental mapping analysis was conducted at the Sinopec Science and Technology Research Center (Bejing, China). The experiments utilized a micro-X-ray fluorescence spectrometer (M4 TORNADO PLUS, manufactured by Bruker, Bremen, Germany, equipped with the AMICS mineral analysis system). This instrument enables non-destructive, high-speed scanning of entire sample areas and elemental distribution imaging of rock samples. The analysis parameters were set as follows: beam spot size: 0.5 mm; step size: 35 μm; excitation voltage: 50 kV; beam current: 600 μA. Following the acquisition of elemental distribution patterns across the surface of individual rock thin sections, mineral distribution information was calculated using the system software (Amics-3.3).

3.3. Petrographic Analysis of Fracture Veins

Petrographic observations of the prepared doubly polished thin sections were conducted under transmitted light (TL), polarized light (PL), and reflected light (RL) at the Key Laboratory of Petroleum Resources and Exploration Technology, Yangtze University (Hubei, China). The observations utilized a Zeiss Axio Imager M2m microscope (Carl Zeiss, Oberkochen, Germany). Additionally, cathodoluminescence (CL) analysis was performed using a NIKON-LV 100 microscope equipped with a CL 8200 MK 5 CL detector. The analysis employed a 2.5x objective lens magnification. The CL operating conditions were set as follows: accelerating voltage: 10.5 kV; beam current: 300 μA; exposure time: 1000 ms.

3.4. Fluid Inclusion Analyses

Analyses related to fluid inclusions were conducted at the Key Laboratory of Petroleum Resources and Exploration Technology, Yangtze University (Hubei, China). Petrographic characterization of fluid inclusions was performed using a ZEISS AXIO Imager D1m microscope (Carl Zeiss, Germany) equipped with transmitted light and ultraviolet light sources (UV excitation wavelength: 365 nm).

Homogenization temperature measurements employed a Linkamd heating–freezing stage (UK). The protocol comprised: preliminary runs at a heating rate of 15 °C/min to identify the approximate homogenization temperature range (bubble disappearance); cooling to room temperature followed by formal runs at 10 °C/min; reduced heating rate (2–3 °C/min) near the pre-determined temperature range for precise measurement. Salinity determination utilized Bodnar's [26] empirical formula based on ice-melting temperatures:

$$\text{Salinity (wt\%NaCl)} = 0.00 + 1.78\theta - 0.0442\theta^2 + 0.000557\theta^3$$

where θ denotes the ice point depression value (°C, relative to 0 °C for pure water). Ice point measurement procedure: initial cooling from room temperature to −50 °C at 5 °C/min to induce crystallization; subsequent warming at 2 °C/min to observe crystal dissolution and bubble movement, recording the final ice-melting temperature.

3.5. In Situ C-O-Sr Isotope Analyses

Analyses were performed at Kehui Testing (Tianjin, China) Co., Ltd. using LA-MC-ICP-MS (RESOlution SE 193 nm laser ablation system coupled with Neoma multicollector ICP-MS).

For the C-O isotope experiment, the calibration standard used was GBW04405, and the quality control sample was GBW04416. The test precision was better than 0.5‰ (1σ), and the test error (accuracy) of the standard sample was $\delta^{13}C‰ < 0.2‰$, $\delta^{18}O‰ < 0.5‰$. Before the experiment, the surface of the thin-section sample was cleaned with hydrogen peroxide. After cleaning, the sample was placed in the sample chamber, which was then sealed and evacuated to below 0.1 Pa using a vacuum pump. Subsequently, helium gas was introduced until the helium flow meter of the system showed a reading of 0, and the vacuum pump was used for evacuation. This operation was repeated 3 times. The sample was heated with a laser with a spot diameter of 100 μm, and the reaction ended in about 8 seconds. A blank experiment control was required every time the sample position was changed. The CO_2 gas produced after the reaction was sequentially carried into the first cold trap (both cold traps were immersed in liquid nitrogen) and the second cold trap by helium carrier gas for concentration, enrichment, and purification, and finally entered the continuous flow of Delta Q for testing. After the test, a vacuum pump was used for evacuation (to below 0.1 Pa) to reduce the memory effect.

In the Sr isotope experiment, the laser energy density was approximately 4.5 J/cm^2, with a frequency of 8 Hz, and the diameter of the ablation spot ranged from 38 to 80 μm. The single-point ablation mode was adopted. The ablated substances were carried out of the sample cell by high-purity He as the carrier gas, mixed with high-purity Ar and N_2, and then entered the mass spectrometer for isotope determination. The flow rate of He gas was about 400 mL/min, and that of N_2 was approximately 5.5 mL/min. For Sr isotopes, a blank was collected for about 10 seconds before laser ablation, with an integration time of 20 seconds. For the Sr isotope data, a ratio of $^{85}Rb/^{87}Rb = 2.593$ was used to deduct the interference of ^{87}Rb on ^{87}Sr. The exponential fractionation law was applied, and $^{87}Sr/^{86}Sr = 8.375209$ was assumed as the internal standard to correct the fractionation of $^{87}Sr/^{86}Sr$.

4. Results

Based on an integrated analysis of core photographs and microscopic observations of rock thin sections, two kinematically distinct types of fracture veins have been identified in the study area, characterized by their physical morphology and cross-cutting relationships with shale bedding (Figure 1d): Bedding-complex fracture veins, characterized by their bedding-parallel development, composite banded morphology hosting mineralization, which is referred to as the BCFV. Y-shaped high-angle fracture veins refers to a high-angle structural fracture where the main fracture branches downward to form two secondary fractures, presenting an inverted Y shape. The inclination angle of the main fracture is greater than 85°, and the branching angle ranges from 25° to 45°, which is called the Y-HFV in this paper. This study focuses on deciphering their differential opening mechanisms.

4.1. BCFV Petrological Characteristics

4.1.1. Elemental Surface Scanning

Micro-XRF elemental mapping of Well Maye 1 (Figure 2) reveals pronounced banding in Al, Fe, K, Si, and S with significant spatial overlap between Mn and Mg domains. Gray-white fracture veins exhibit dominant Si-Ca-Mg signatures, indicating infilling by gangue minerals (quartz, calcite, dolomite), while the black shale matrix contains Al-Fe-K-Mn-Si-S-Na, suggesting constituents of clay minerals, alkali-bearing minerals, and Fe-rich metallic minerals. Specifically, silicon distribution displays three distinct bands: two narrower equidistant dilation fractures on the left, one heterogeneous dissolution-modified dilation fracture with variable width on the right, and point-like clusters in central areas; calcium distribution features blocky intercalations in central zones with an elongated vein cross-cutting Si-rich bands in the upper right; magnesium distribution partially overlaps calcium-enriched domains in lighter hues. The composite element map demonstrates fracture veins comprising three mineral-specific zones: green (quartz-dominated), red (calcite-rich), and pink (dolomite-concentrated). All matrix elements (Al, Fe, K, Mn, Si, S) show preferential bedding-parallel alignment, except irregularly distributed Na and Cl.

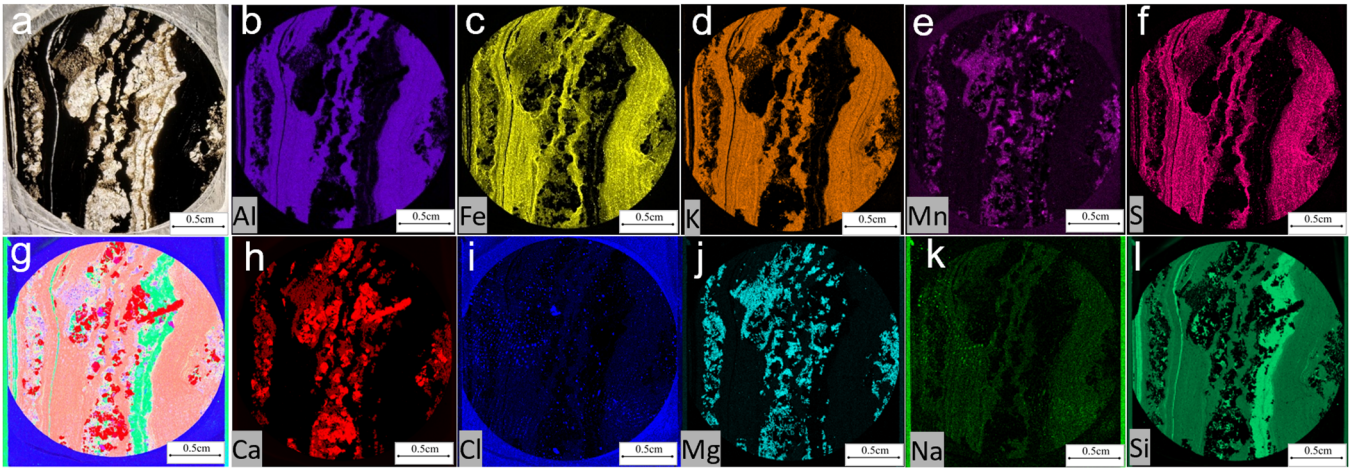


Figure 2. Photomicrographs and elemental mapping distribution of BCFV in Well Maye 1. (**a**) Panoramic view of bedding-parallel fracture veins; (**b**) aluminum (Al) elemental mapping; (**c**) iron (Fe) elemental mapping; (**d**) potassium (K) elemental mapping; (**e**) manganese (Mn) elemental mapping; (**f**) sulfur (S) elemental mapping; (**g**) composite elemental map; (**h**) calcium (Ca) elemental mapping; (**i**) chlorine (Cl) elemental mapping; (**j**) magnesium (Mg) elemental mapping; (**k**) sodium (Na) elemental mapping; (**l**) silicon (Si) elemental mapping.

4.1.2. Cathodoluminescence of Fracture Veins

Integrated Interpretation of Bedding-Parallel Fracture Veins in Well Maye 1 (Figure 3): Transmitted and cathodoluminescence (CL) imagery reveal a well-defined polyphase mineralization sequence within the fracture veins, comprising early-stage quartz, intermediate calcite, and late-stage dolomite. Cross-cutting relationships demonstrate that intermediate calcite veins truncate early quartz veins, indicating later fracture infilling, while late dolomite progressively replaces calcite and quartz along the fractures. Calcite and dolomite exhibit petrographic similarity with interdigitated contacts in localized zones, suggesting a transitional genetic link during their precipitation (Figure 2g). Under transmitted light (Figure 3a,e), quartz appears translucent and pristine, whereas dolomite displays darker gray hues compared to calcite. Diagnostic CL responses show calcite emitting a dull red luminescence, contrasting sharply with dolomite's vivid orange-red emission, while both quartz and the host rock remain non-luminescent (Figure 3b,c,f,g). Because CL emission in carbonates is primarily controlled by the concentration of activators (Mn^{2+}) and quenchers

(Fe^{2+}), the distinct shift from non-luminescent quartz to dull red calcite, and finally to bright orange-red dolomite, strongly suggests a staged fluid geochemical evolution marked by progressively increasing Mn^{2+}/Fe^{2+} ratios. These CL characteristics, integrated with the textural sequence, indicate at least three discrete fluid flow events rather than a single continuous diagenetic process.

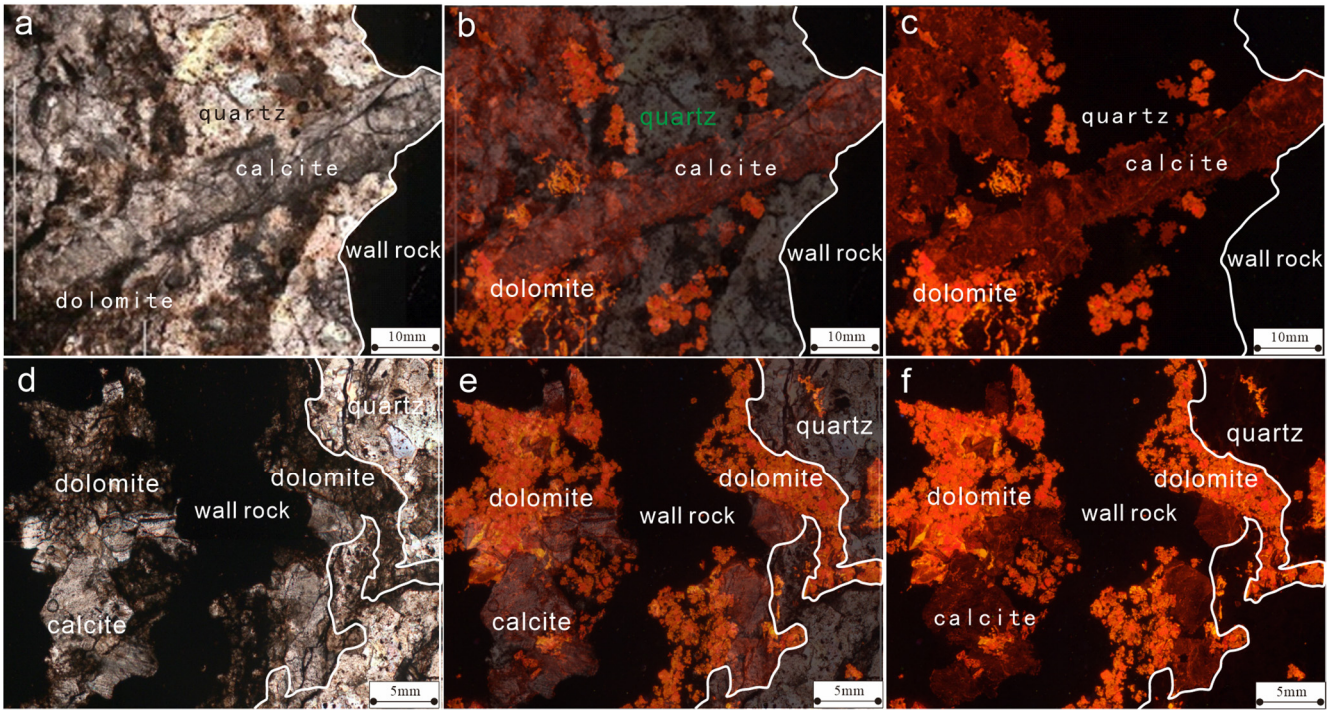


Figure 3. Photomicrographs and cathodoluminescence imagery of BCFV in Well Maye 1. (**a**–**c**) Mineral infill comprising quartz, calcite, and dolomite at 4820.17 m; (**a**) transmitted light image showing calcite veins cross-cutting quartz; (**b**) transmitted–cathodoluminescence overlay; (**c**) cathodoluminescence image; (**d**–**f**) dolomite replacement of calcite and quartz at 4820.17 m; (**d**) transmitted light image documenting replacement textures; (**e**) transmitted–cathodoluminescence overlay; (**f**) cathodoluminescence image. Note: quartz–host rock boundaries are outlined by white rims for clarity.

4.1.3. Types and Distributions of Fracture Vein Minerals

Mineralogical Quantification of BCFV via AMICS Analysis (Bruker System): Due to the nature of AMICS mapping, which targets specific regions of interest (ROIs) within a single thin section, standard deviations across multiple thin sections are not applicable. Therefore, it is important to clarify that the AMICS results reported herein represent the precise modal abundances of the analyzed fracture domains, rather than bulk rock averages. It should be noted that the AMICS results are reported as area percentages (area %), which is the standard output format for 2D thin-section mapping analyses. Integrated petrographic and elemental mapping reveals the following mineral abundance in descending order (Figure 4): clay matrix (46.64%), quartz (15.96%), calcite (13.68%), dolomite (10.75%), barytocalcite, laumontite, pyrite, reedmergnerite, wollastonite, and various mineral intergrowths (e.g., barytocalcite–quartz and pyrite–calcite). Specifically, the smectite-dominated shale matrix constitutes 46.64% of the mapped area (Figure 4c). Within this groundmass, rigid minerals (primarily pyrite) and organic matter are predominantly aligned parallel to the bedding, though some are randomly disseminated. Spatially, quartz veins (15.96%) are concentrated in the right sector of the thin section, whereas calcite (13.68%) and dolomite (10.75%) collectively occupy the central fracture domain (Figure 4d–f).

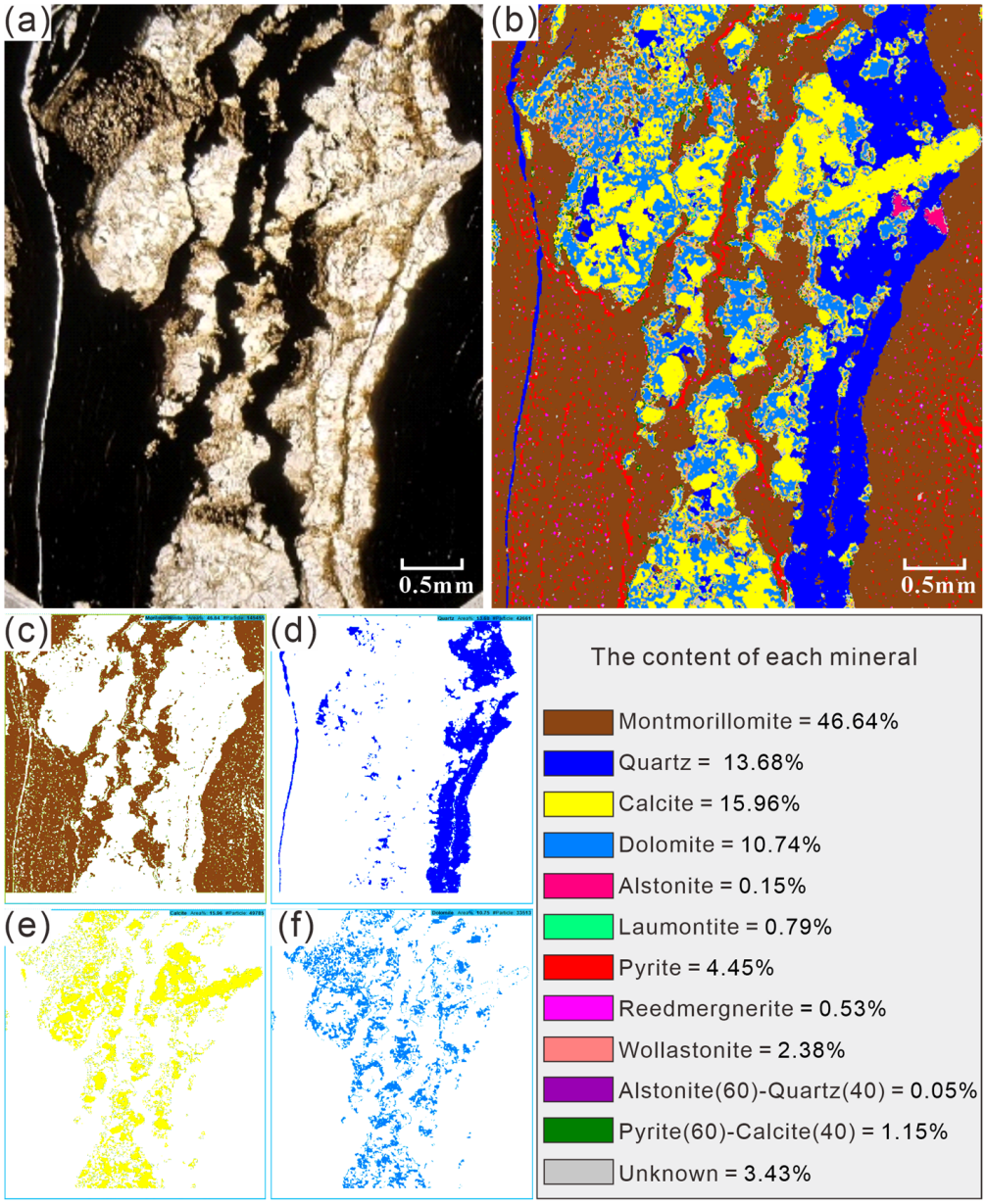


Figure 4. Distribution and content of fracture vein minerals in Well MY1 based on elemental analysis. (**a**) Transmitted light image; (**b**) mineral assemblage; (**c**) shale matrix distribution and proportion image; (**d**–**f**) distribution and proportion of minerals in the main vein.

4.2. Y-HFV Petrological Characteristics

4.2.1. Elemental Surface Scanning

Integrated Micro-XRF Mapping of Well Fengcheng 1 (Figure 5): Elemental mapping demonstrates Ca and Cl exclusively localized within fracture veins, while Al, Fe, K, and S exhibit pronounced banding with significant spatial overlap between Fe and K domains. The black shale matrix contains Al-Fe-K-Mn-Si-S, consistent with typical clay mineral compositions (illite, feldspars). Gray-white veins displaying chevron patterns are dominated by Ca-Cl-Mg-Na signatures, indicating infilling by carbonates and alkali-bearing minerals. Spatial analysis reveals calcium occupying the primary vein volume with complementary Na-Ca zoning. The composite element map distinguishes two mineralogical phases: orange (carbonate-dominated zones) and blue (alkali mineral concentrations).

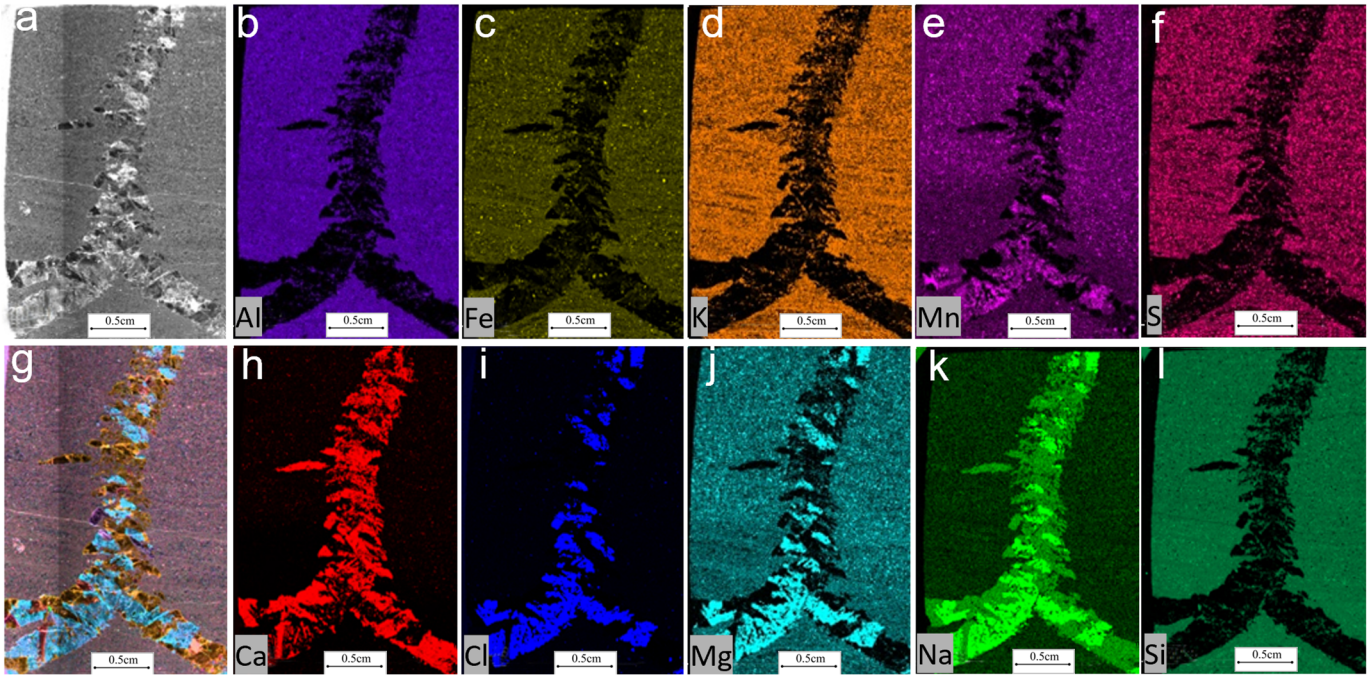


Figure 5. Photomicrographs and elemental mapping distribution of Y-HFV in Well Fengcheng 1. (**a**) Panoramic view of bedding-parallel fracture veins; (**b**) aluminum (Al) elemental mapping; (**c**) iron (Fe) elemental mapping; (**d**) potassium (K) elemental mapping; (**e**) manganese (Mn) elemental mapping; (**f**) sulfur (S) elemental mapping; (**g**) composite elemental map; (**h**) calcium (Ca) elemental mapping; (**i**) chlorine (Cl) elemental mapping; (**j**) magnesium (Mg) elemental mapping; (**k**) sodium (Na) elemental mapping; (**l**) silicon (Si) elemental mapping.

4.2.2. Cathodoluminescence of Fracture Veins

Transmitted light microscopy and cathodoluminescence (CL) characteristics of the fracture-filling veins in the Y-HFV (Well Fengcheng 1) are depicted in Figure 6. Because CL emission in minerals is highly sensitive to trace element variations (particularly Mn^{2+} and Fe^{2+} activators and quenchers), the CL responses provide critical insights into the exceptionally complex fluid-mediated alteration within these veins. Under CL, the host rock matrix appears dark, scattered with isolated red and violet-blue speckles, likely representing trace element-enriched detrital phases.

The calcite veins exhibit rhythmic, banded orange-yellow luminescence with core-to-rim intensity variations. These oscillatory CL textures strongly suggest fluctuating trace element concentrations (e.g., Mn^{2+}/Fe^{2+} ratios) during crystallization, pointing to a pulsed hydrothermal fluid influx rather than continuous precipitation. Furthermore, the irregular vein morphology, stark CL contrast with the matrix, and diffuse red luminescent halos along the vein margins (Figure 6a,b) are consistent with an epigenetic hydrothermal origin and pervasive fluid–rock interaction. In transmitted light, the distinct optical properties of the vein minerals are clear: calcite displays well-defined grain boundaries and vivid interference colors, contrasting sharply with the dark, irregular, and rough-surfaced northupite [$Na_2Mg(CO_3)_2Cl_2$] (Figure 6c).

Integrated CL and petrographic analyses identify calcite and northupite as the dominant vein minerals, with their heterogeneous CL responses indicating a dynamic fluid composition and multi-stage evolution (Figure 6d):

① Calcite: Exhibits weak brownish-yellow to pale orange luminescence, implying a relatively low concentration of Mn^{2+} activators within its crystal lattice. The fibrous CL textures along the rock contacts further support episodic fluctuations in fluid chemistry during vein growth.

② Northupite: Displays dull to dark red luminescence, suggesting an uneven incorporation of CL activators (e.g., Mn, Fe) within its complex Na-Mg-Cl-CO_3 structure. The irregular CL morphology of northupite, which aligns with its rough surface texture in transmitted light, indicates complex crystallization conditions or potential late-stage fluid reworking.

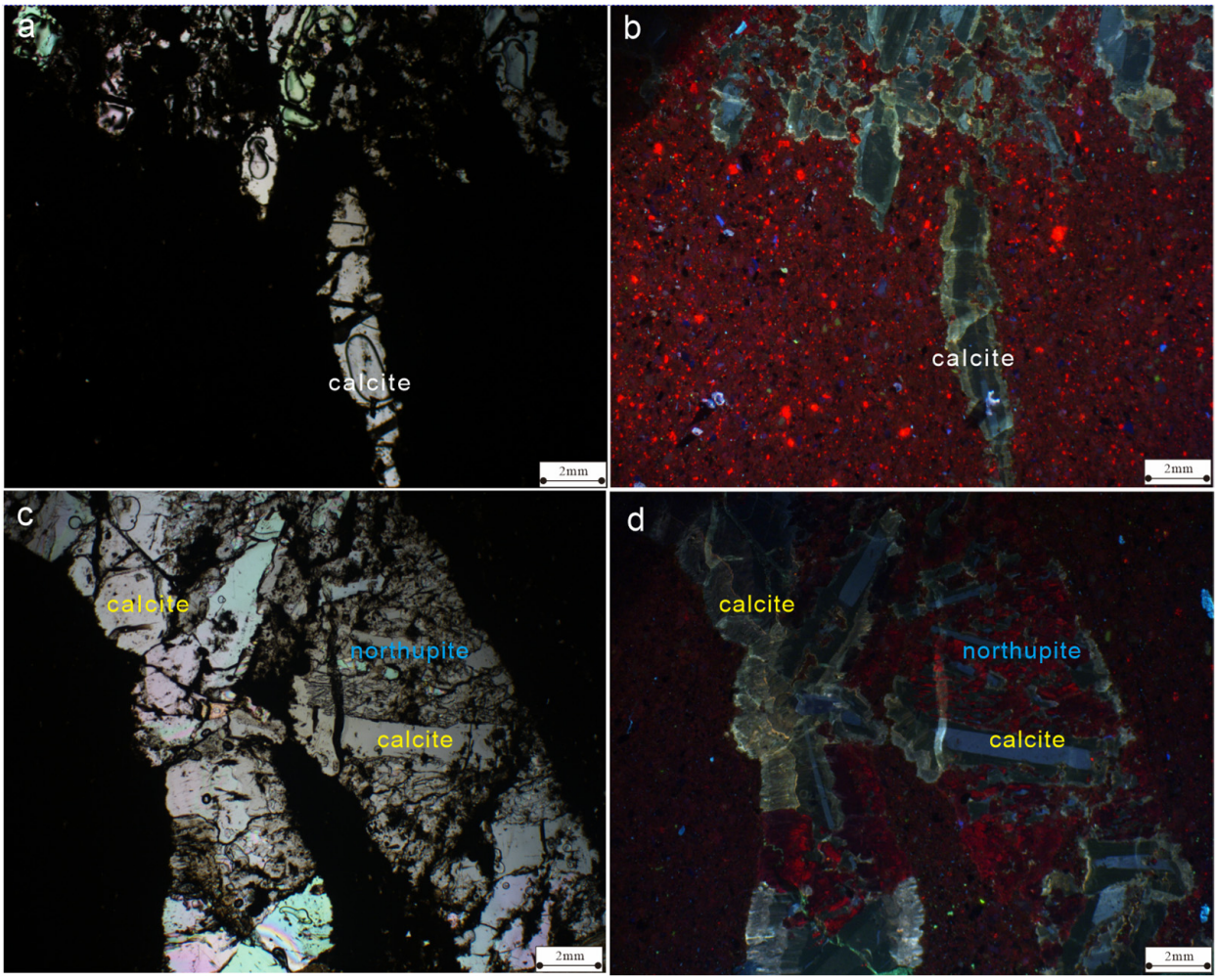


Figure 6. Photomicrographs and cathodoluminescence imagery of Y-HFV in Well Fengcheng 1. (**a**,**b**) Micro-fractures filled with calcite veins: (**a**) Transmitted light image; (**b**) cathodoluminescence (CL) image; (**c**,**d**) fractures filled with calcite and northupite veins: (**c**) transmitted light image; (**d**) cathodoluminescence (CL) image.

4.2.3. Types and Distribution of Fracture Vein Minerals

Mineralogical Quantification of Y-HFV via AMICS Analysis (Bruker System): Utilizing the AMICS (Automated Mineral Identification and Characterization System) developed by Bruker, Germany, the areal distribution and mineral content of the Y-HFV were quantitatively evaluated by integrating petrographic observations with elemental mapping (Figure 7). The results reveal the following mineral abundance in descending order: illite (51.06%), calcite (13.22%), northupite (6.89%), ferroan calcite, pyrite, albite, wollastonite, orthoclase, anorthoclase, reedmergnerite, quartz, dolomite, and shortite. The clay-dominated matrix, consisting primarily of illite, constitutes 51.06% of the mapped area (Figure 7c). Calcite and northupite form the primary fracture infillings (13.22% and 6.89%, respectively). Within the Y-HFV, these minerals develop vertically, cross-cutting the host rock bedding, and exhibit an intercalated distribution along dissolution fractures (Figure 7d,e).

Minor ferroan calcite is also observed along the margins of the calcite veins (Figure 7f). Detrital dolomite and quartz grains are randomly disseminated throughout the clay matrix, whereas feldspar grains (albite, anorthoclase, and orthoclase) align subparallel to the shale bedding.

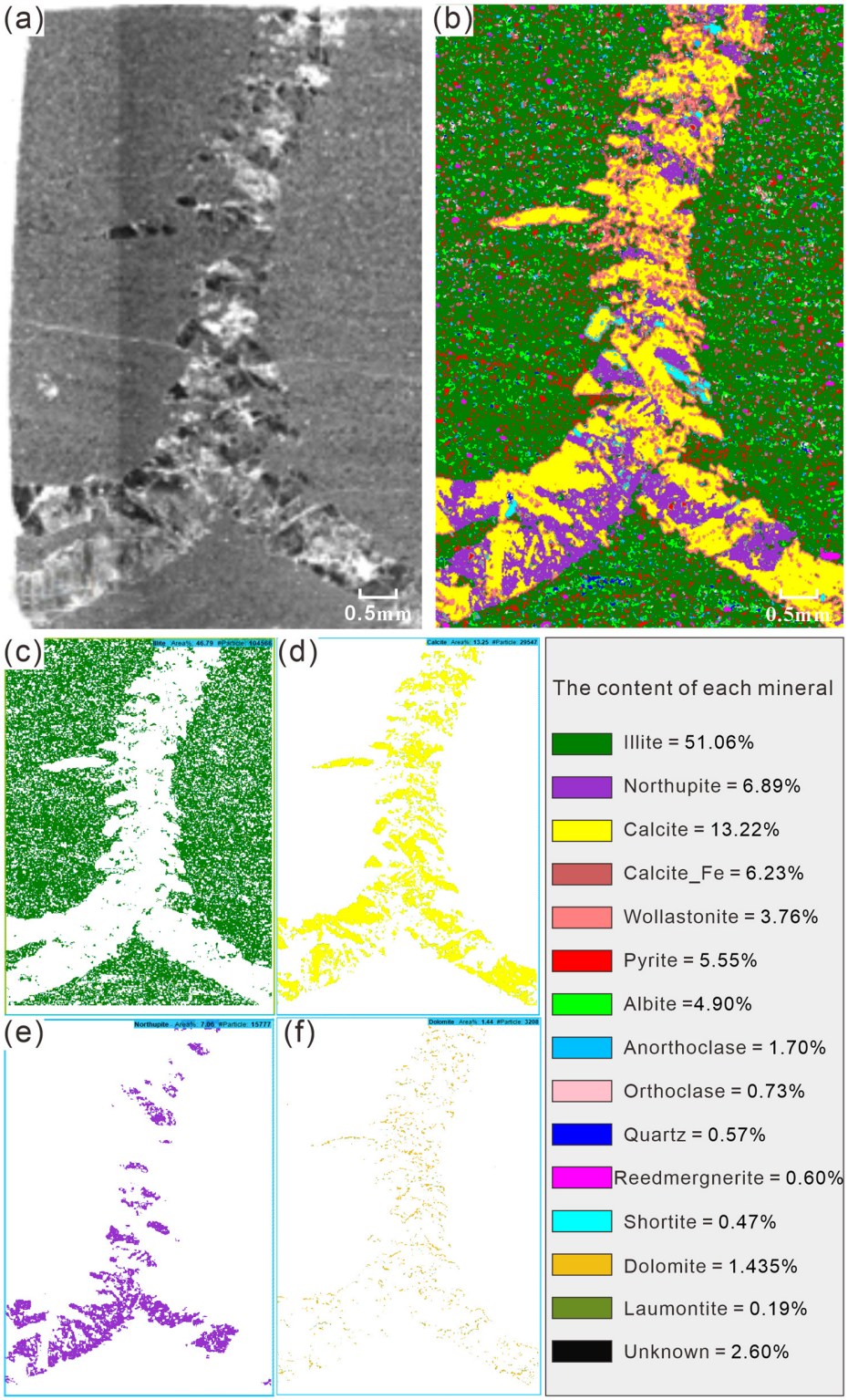


Figure 7. Distribution and content of fracture vein minerals in Well FC1 based on elemental analysis. (**a**) Transmitted light image; (**b**) mineral assemblage; (**c**) shale matrix distribution and proportion image; (**d**–**f**) distribution and proportion of minerals in the main vein.

4.3. Geochemical Signatures of Fracture Veins

4.3.1. Carbon–Oxygen Isotopic Signatures of Fracture Veins

The carbon and oxygen isotope characteristics of the fracture veins in the Fengcheng Formation of Well Maye 1 and Well Fengcheng 1 are shown in Figure 8. Since quartz veins lack carbon and oxygen for isotopic analysis, only calcite and dolomite within the bedding-complex fracture veins (BCFVs) were analyzed for their carbon–oxygen isotopic signatures. BCFV dolomite exhibits predominantly positive $\delta^{13}C_{V\text{-}PDB}$ values, ranging from −0.02‰ to +2.91‰. For BCFV calcite, the $\delta^{13}C_{V\text{-}PDB}$ values range from −1.77‰ to +1.35‰, with a single negative outlier (−1.77‰); excluding this outlier, its isotopic signature aligns closely with dolomite, though within a narrower range compared to dolomite. Minimal $\delta^{13}C_{V\text{-}PDB}$ divergence exists between these two vein minerals. In summary, the $\delta^{13}C_{V\text{-}PDB}$ values show negligible divergence between the two vein minerals. BCFV dolomite $\delta^{18}O_{V\text{-}PDB}$ ranges from −3.12‰ to −10.54‰, whereas BCFV calcite $\delta^{18}O_{V\text{-}PDB}$ exhibits distinctly depleted values ranging from −11.84‰ to −13.31‰.

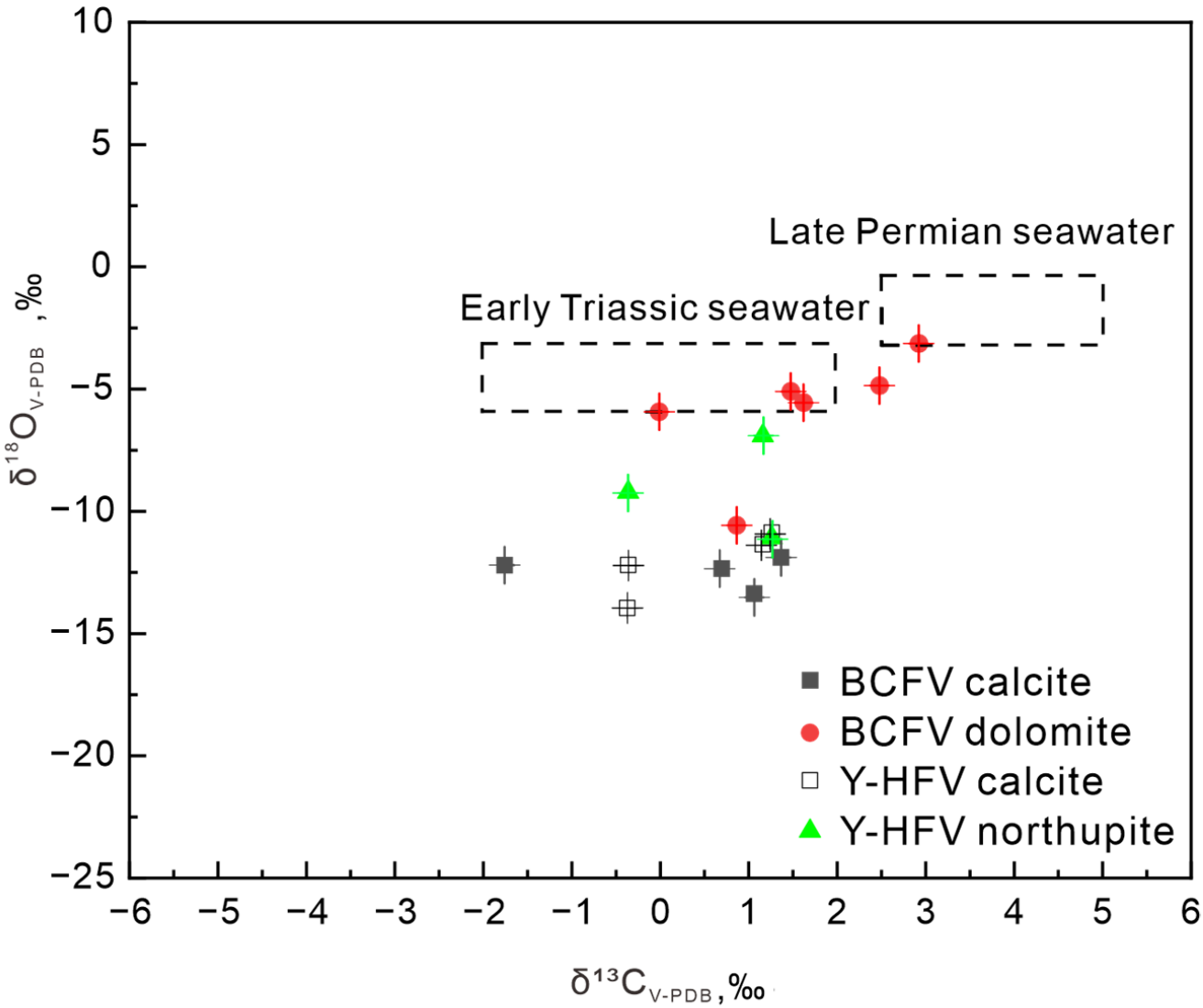


Figure 8. Crossplot between $\delta^{18}O$ and $\delta^{13}C$ values in fracture vein. Reference for seawater range data in different periods [27].

Within the Y-HFV, mineralization is dominated by calcite and northupite. The $\delta^{13}C_{V\text{-}PDB}$ values of the Y-HFV calcite range from −0.37‰ to +1.25‰, largely overlap-

ping with the $\delta^{13}C_{V\text{-}PDB}$ range of the BCFV dolomite. The Y-HFV northupite exhibits more negative $\delta^{13}C_{V\text{-}PDB}$ values than the Y-HFV calcite, ranging from −4.42‰ to −1.24‰. The $\delta^{18}O_{V\text{-}PDB}$ variation range of the Y-HFV calcite is from −13.91‰ to −10.84‰, and the $\delta^{18}O_{V\text{-}PDB}$ variation range of the Y-HFV northupite is from −11.03‰ to −6.88‰. As evidenced in Figure 8, the C-O isotopic signatures of the BCFV dolomite plot within the transitional zone between Early Triassic and Middle–Late Permian paleo seawater composition fields, BCFV calcite, Y-HFV calcite, and Y-HFV northupite exhibit significant deviations from coeval seawater C-O isotopic fields, characterized by marked depletion in the $\delta^{18}O_{V\text{-}PDB}$ values.

4.3.2. Strontium Isotopic Characteristics of Fracture Veins

As illustrated in Figure 9, the $^{87}Sr/^{86}Sr$ ratios of calcite (0.70554–0.70568) and dolomite (0.70567–0.70574) in bedding-concordant fracture veins (BCFVs) are consistently lower than those of the host rock (0.70585–0.70616). The $^{87}Sr/^{86}Sr$ ratios of host rock samples 11–14 from the BCFV range from 0.70559 to 0.70618, with Sample 13 (0.70618) being notably higher than the others. In the Y-HFV, the $^{87}Sr/^{86}Sr$ ratios of calcite fall within 0.70537 to 0.70567, exhibiting a certain degree of dispersion while remaining within a specific interval. Northupite exhibits $^{87}Sr/^{86}Sr$ ratios of 0.70487–0.70546, characterized by a progressive depletion trend. Host rock ratios range from 0.70617 to 0.70612, representing the highest values among all samples while remaining consistent with the BCFV host lithologies. Overall, different types of veins exhibit variations in their $^{87}Sr/^{86}Sr$ ratios, indicating potential differences in their formation environments, material sources, or geological processes.

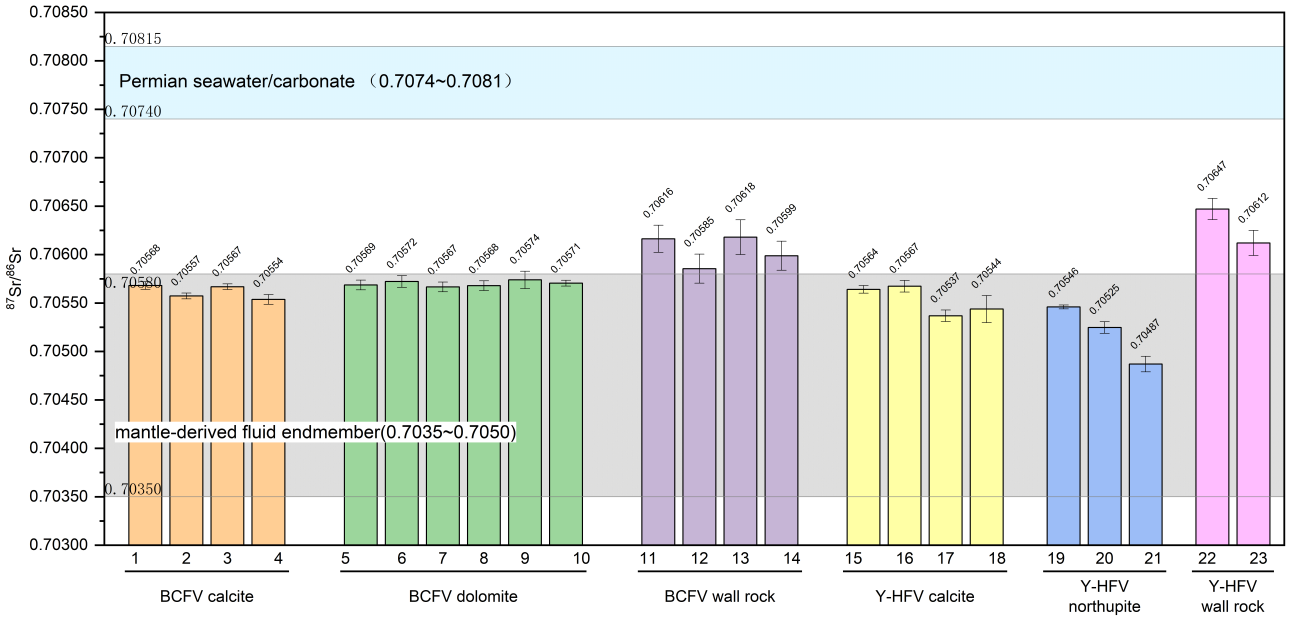


Figure 9. $^{87}Sr/^{86}Sr$ ratios in fracture-filling veins. (Error bars represent 2σ analytical uncertainties).

4.4. Evidence of Fluid Inclusions in Fracture Veins

The Permian Fengcheng Formation shale fractures within the Mahu Sag study area contain quartz, calcite, dolomite, and some northupite fracture-filling veins, all hosting diverse fluid inclusions. Hydrocarbon inclusions significantly outnumber aqueous inclusions in most veins, with calcite ($CaCO_3$) exhibiting the most abundant inclusions, followed by quartz (SiO_2). These include primary and secondary hydrocarbon inclusions, bitumen inclusions, gaseous hydrocarbon inclusions, minor aqueous inclusions, and three-phase (gas–liquid–solid) fluid inclusions. Primary inclusions were trapped along growth zones of

host minerals during precipitation and are observed within healed lattice planes of calcite and quartz. Other gaseous and aqueous inclusions distributed along healed fractures are typically identified as secondary inclusions.

4.4.1. Primary Inclusions in BCFV Quartz

As shown in Figure 10, under the microscope, various types of inclusions are developed in the BCFV quartz, including liquid hydrocarbon inclusions that emit blue-green fluorescence, bitumen inclusions, bitumen-bearing aqueous inclusions, and a small amount of common aqueous inclusions. The majority of primary hydrocarbon and aqueous inclusions occur along growth zones within the minerals, while a minority exist as isolated inclusions in the crystals. Secondary inclusions typically manifest as small clusters or in banded patterns. The fluid inclusions within the quartz veins exhibit diameters ranging from 10 μm to 25 μm, with rectangular, rhombic, and elliptical morphologies being the most prevalent. Hydrocarbon and bitumen inclusions within quartz veins exhibit significantly larger diameters and higher abundances compared to those in calcite and dolomite veins. The primary three-phase (gas–liquid–solid) fluid inclusions containing solid bitumen, liquid hydrocarbons, and gaseous hydrocarbons indicate post-entrapment evolution of the captured hydrocarbons. This demonstrates that the early-charged liquid hydrocarbons trapped within the quartz veins underwent thermal cracking evolution during late-stage deep burial processes.

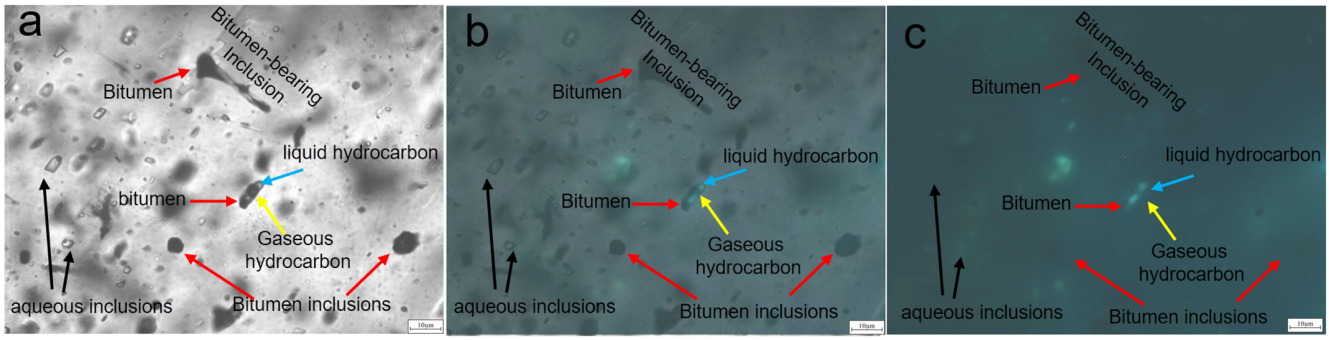


Figure 10. Photomicrographs of primary fluid inclusions in quartz from BCFV. (**a**) Transmitted light photomicrograph of primary fluid inclusions in quartz veins; (**b**) overlay image of transmitted light and fluorescence showing primary fluid inclusions in quartz veins; (**c**) fluorescence photomicrograph of primary fluid inclusions in quartz veins.

4.4.2. Primary Inclusions in BCFV Calcite

The calcite in the BCFV hosts abundant bitumen inclusions and liquid hydrocarbon inclusions, predominantly distributed as clusters along growth zones. Most are primary inclusions, with measured diameters ranging from 5 to 13 μm under microscopy. Morphologies include elliptical, rod-shaped, trapezoidal, rectangular, and subhedral to anhedral forms. While hydrocarbon and bitumen inclusions in quartz veins (Qtz) exhibit considerably larger diameters, calcite veins (Cc) in the BCFV contain significantly higher abundances of these inclusions. Moreover, exclusively in calcite veins, liquid hydrocarbon inclusions exhibit yellow-green fluorescence under ultraviolet (UV) excitation, suggesting the presence of immature hydrocarbons (see Figure 11a). In contrast, the vast majority of hydrocarbon inclusions within the fracture-filling veins display blue-green to pale blue fluorescence (Figure 11c,f). Comparison of Figure 11b,c reveals abundant blue-green fluorescent liquid hydrocarbon inclusions within calcite veins. In contrast, dolomite veins lack any observable fluorescence and exhibit sparsely developed inclusions of other types. Figure 11d reveals deformed and elongated bitumen inclusions distributed along growth zones of the vein, accompanied by secondary bitumen inclusions with well-defined trapezoidal

morphologies and associated aqueous inclusions. Bitumen inclusions appear opaque black under transmitted light microscopy and exhibit negative fluorescence under ultraviolet (UV) excitation (Figure 11e,f).

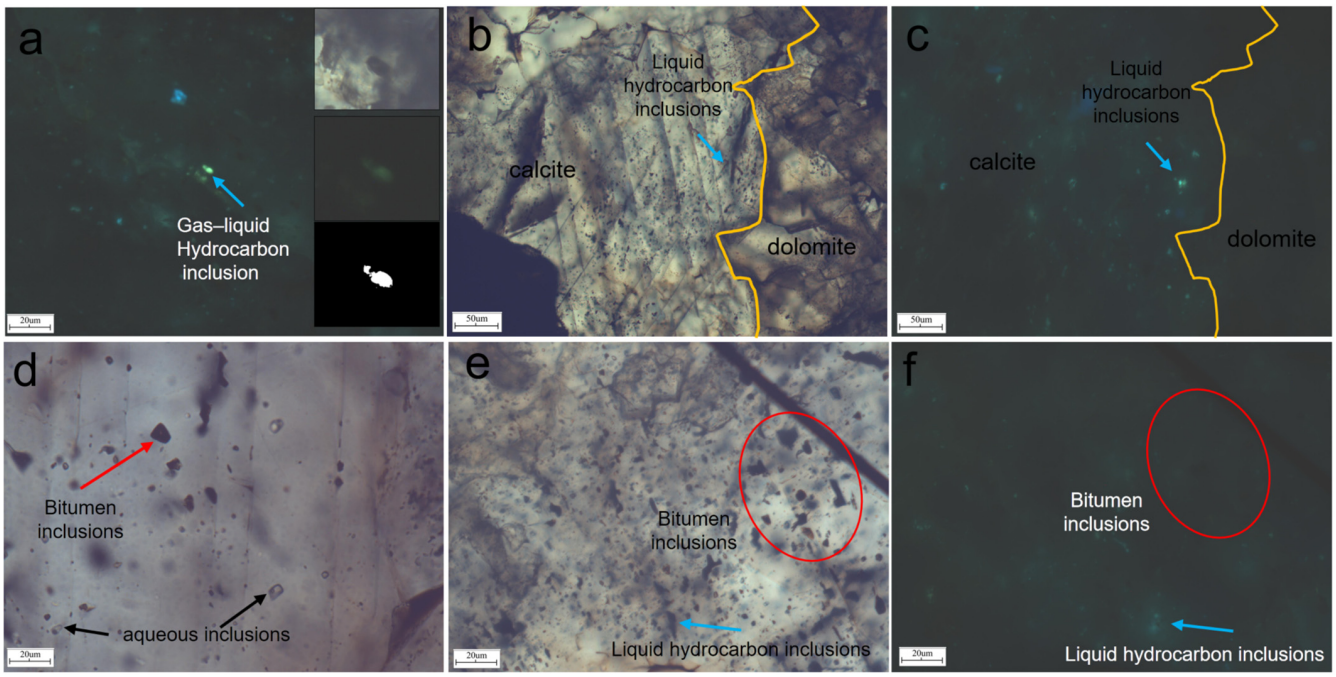


Figure 11. Photomicrographs of fluid inclusions in calcite from BCFV. (**a**) Fluorescence image at 20× magnification showing immature yellow-green fluorescent gas–liquid hydrocarbon inclusions in calcite vein. Right panel (top to bottom): 50× transmitted light image, fluorescence image, and liquid hydrocarbon proportion image; (**b**) secondary gaseous hydrocarbon inclusions and bitumen inclusions in calcite vein at 20× magnification; (**c**) secondary gaseous hydrocarbon inclusions and aqueous inclusions in dolomite vein at 50× magnification. (**d**) In the calcite vein under the 50× magnification, deformed and elongated bitumen inclusions coexist with regular trapezoidal secondary bitumen inclusions; (**e**) bitumen inclusions and a small amount of liquid hydrocarbon inclusions under 20× magnification; (**f**) Bitumen inclusions show no fluorescence after ultraviolet excitation in the same field of view.

4.4.3. Secondary Inclusions in BCFV Dolomite Veinlets

Microscopic examination reveals striking contrasts between dolomite and adjacent calcite in the BCFV. Dolomite veins exhibit a marked reduction in both the abundance and size of all inclusion types, with hydrocarbon-bearing inclusions being predominantly absent across most domains. These veins are instead dominated by non-fluorescent gaseous hydrocarbon inclusions (Figures 11b,c and 12a,b). The inclusions measure 3~5 μm in size, predominantly exhibiting elliptical to subrounded morphologies. At room temperature (25 °C), they maintain a homogeneous liquid phase without vapor bubble formation, while aqueous inclusions are sparsely developed. Figure 12 reveals bitumen inclusions exhibiting opaque black coloration under transmitted light, occurring along healed fractures within dolomite crystals. These are classified as secondary inclusions. The sparse distribution of hydrocarbon inclusions in dolomite veins likely indicates that the peak hydrocarbon generation phase in the source rock had already ceased.

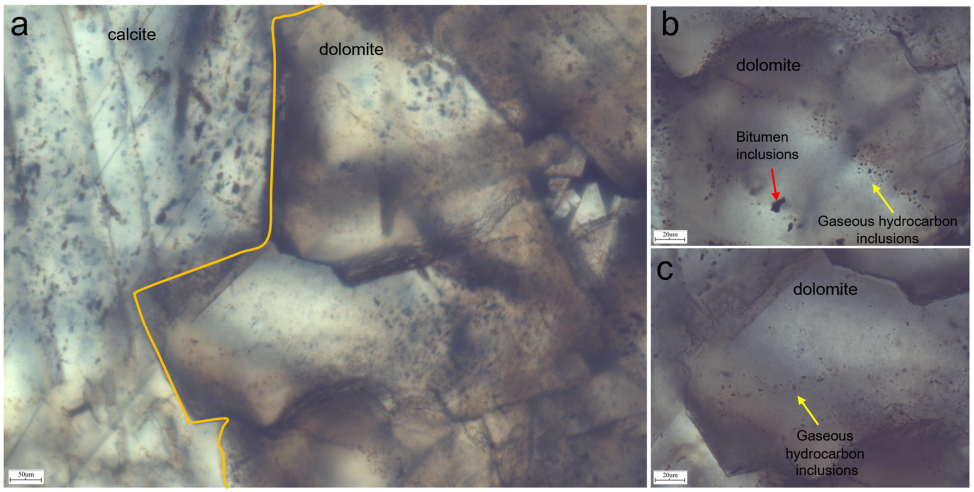


Figure 12. Photomicrographs of secondary inclusions in dolomite from BCFV. (**a**) Transmitted light image at 20× magnification showing calcite and dolomite veins; (**b**) secondary gaseous hydrocarbon inclusions and bitumen inclusions in dolomite vein at 50× magnification; (**c**) secondary gaseous hydrocarbon inclusions and aqueous inclusions in dolomite vein at 50× magnification.

4.4.4. Secondary Inclusions in Y-HFV Calcite

The calcite in the Y-HFV predominantly hosts liquid hydrocarbon inclusions, which distribute as linear arrays along growth zones. Microscopic measurements indicate inclusion diameters of approximately 3~6 μm, with elliptical and rod-shaped morphologies being predominant. Figure 13a,b display liquid hydrocarbon inclusion assemblages (FIAs) exhibiting blue-white fluorescence that transect crystal boundaries, indicating this fluid event postdates calcite precipitation. Figure 13c,d show primary hydrocarbon inclusions with vapor–liquid biphasic characteristics, characterized by yellow-green fluorescence. These inclusions measure 12 μm in diameter with notably high vapor-to-liquid ratios (V/L ≈ 30~40%). Adjacent to these are small-sized secondary liquid hydrocarbon inclusions exhibiting yellow-green fluorescence, aligned along growth zones of the vein. Liquid hydrocarbon inclusions exhibiting yellow-green fluorescence are observed on mineral grains within the host rock, displaying rod-shaped and subrounded morphologies.

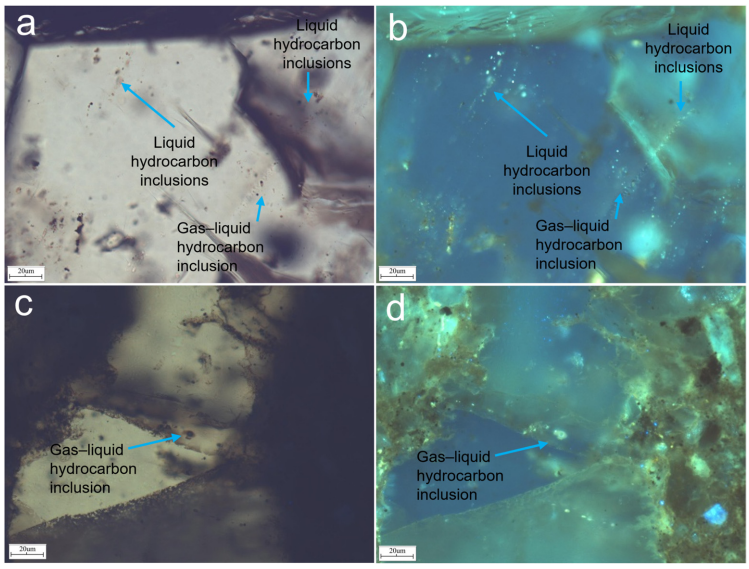


Figure 13. Photomicrographs of secondary inclusions in calcite from Y-HFV. (**a**,**c**) Transmitted light images at 50× magnification showing liquid hydrocarbon inclusions in calcite veins; (**b**,**d**) fluorescence images at 50× magnification of liquid hydrocarbon inclusions in calcite veins.

4.4.5. Secondary Inclusions in Y-HFV Northupite

The Y-HFV northupite contains abundant hydrocarbon inclusions, exhibiting zonal and clustered distributions. The diameters of these inclusions (11–19 μm) are significantly larger than those in the surrounding calcite veins, primarily displaying elliptical and strip-shaped morphologies. Liquid hydrocarbon inclusions appear colorless to light brown, with the light brown coloration generally indicative of low maturity. Under UV fluorescence illumination, these liquid hydrocarbon inclusions exhibit yellow-green fluorescence. Figure 14a shows liquid hydrocarbon inclusions stretched toward the host rock by lateral stress, potentially suggesting that the veins continued propagating toward the host rock under tectonic or other stress conditions. Under transmitted light, bitumen inclusions appear jet black with sharp boundaries (Figure 14c). Some bitumen inclusions exhibit stress-induced elongation into elongated shapes.

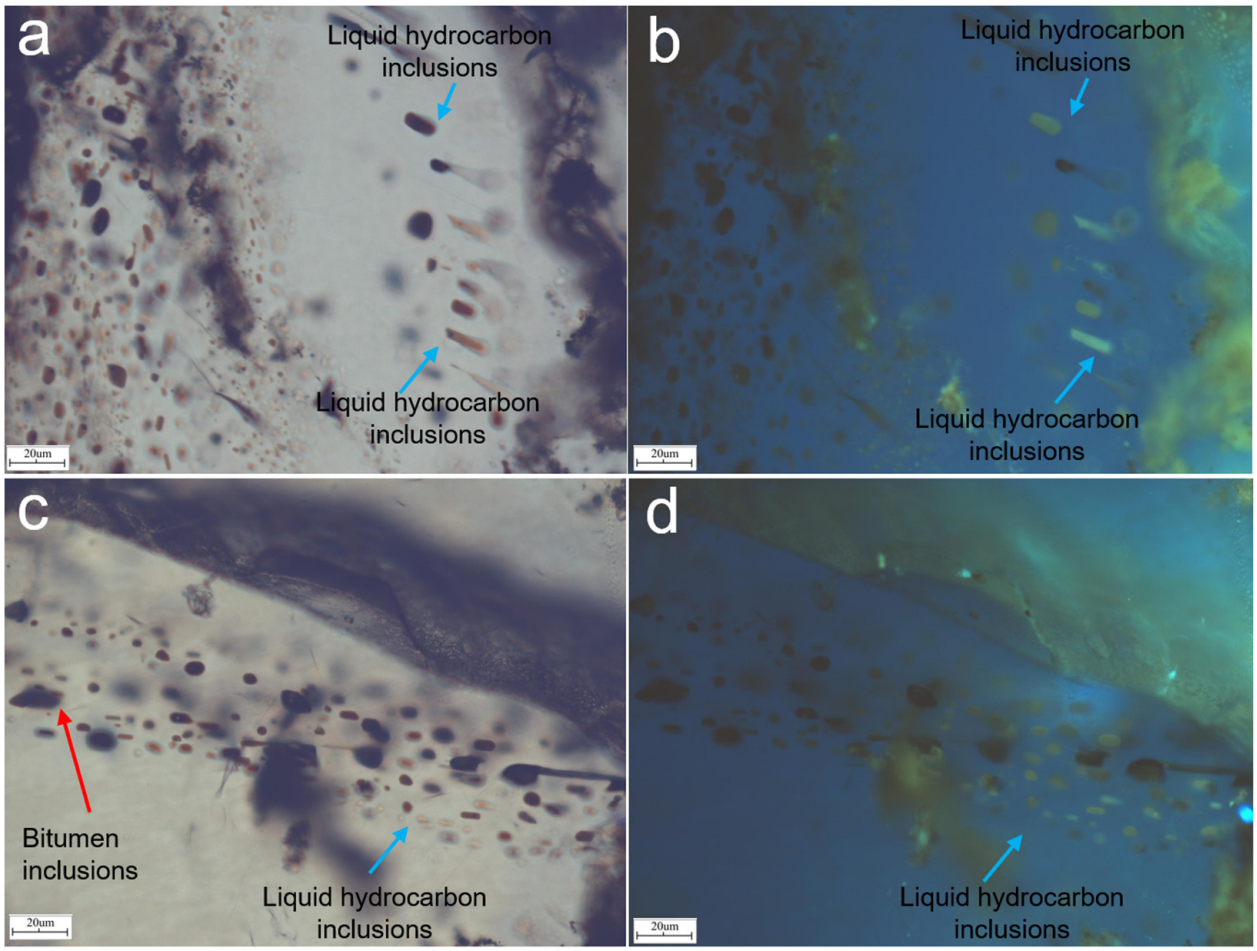


Figure 14. Photomicrographs of secondary inclusions in northupite from Y-HFV. (**a**,**c**) Transmitted light photomicrographs at 50× magnification showing liquid hydrocarbon and bitumen inclusions in calcite veins; (**b**,**d**) fluorescence images at 50× magnification of the same inclusion assemblages in calcite veins.

4.4.6. Temperature and Salinity Characteristics in Fracture Veins

For the BCFV, the T_h of the primary aqueous inclusions (n = 12) in the first-stage quartz vein is mainly 48.1~72.3 °C, with an average of 58.6 °C. The freezing point ranges from −6.5 to −2.6 °C, with an average of −4.9 °C, corresponding to a salinity of 7.7 wt% NaCl. Primary aqueous inclusions (n = 10) in the second-stage calcite veins exhibit T_h ranging from 49.2 to 81.1 °C (peaking at 62.1~75.3 °C). Secondary aqueous inclusions (n = 14) in the third-stage dolomite veins display T_h ranging from 67.1 to 102.5 °C (predominantly

81.4 ~ 91.7 °C; average 84.4 °C). The ice-melting temperatures range from −18.6 to −11.9 °C (average −15.6 °C), corresponding to a salinity of 19.1 wt% NaCl. The T_h and salinity data of these aqueous inclusions (Figure 15) reveal three distinct temperature–salinity clusters, indicating significantly different fluid conditions during the formation of quartz, calcite, and dolomite veins. Primary inclusions in quartz veins exhibit a broad Th range, calcite and dolomite show comparable salinity values, and the three vein stages demonstrate progressively increasing salinity.

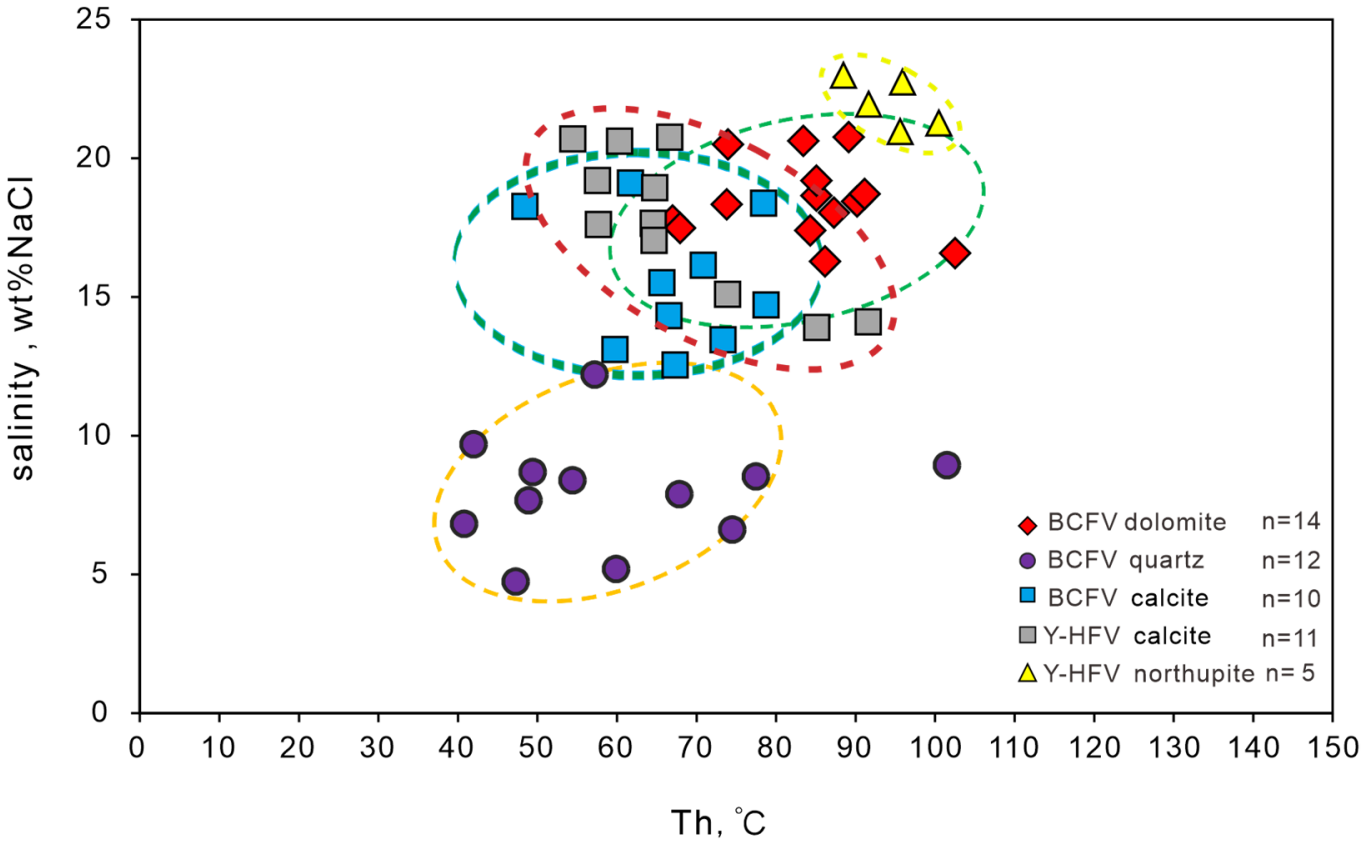


Figure 15. Temperature–salinity crossplot of fluid inclusions.

For the Y-HFV, the Th of calcite aqueous inclusions ranges from 55.4 to 93.2 °C (with an average of 71.2 °C), the freezing point ranges from −16.3 to −9.1 °C (with an average of −12.1 °C), and the corresponding salinity is 16.1 wt% NaCl. The Th of northupite aqueous inclusions ranges from 91.7 to 103.8 °C (with an average of 95.6 °C), the freezing point ranges from −23.6 to −17.4 °C, with an average of −21.5 °C, and the corresponding salinity is 23.4 wt% NaCl. The data (Figure 15) reveal that both exhibit substantial variations in homogenization temperatures, while northupite displays markedly higher salinity than calcite in contrast.

5. Discussion

5.1. Fracture Vein Types and Opening Mechanisms

5.1.1. C-O-Sr Isotopic Signatures of Fracture Veins

Carbon and oxygen isotopes serve as robust proxies for tracing diagenetic fluids. As shown in Figure 8 (where analytical uncertainties of ±0.2‰ for both $\delta^{13}C$ and $\delta^{18}O$ are indicated by error bars), most carbonate minerals filling both the BCFV and Y-HFV exhibit C-O isotopic compositions that deviate from the Permian–Triassic seawater range, with only minor dolomite in the BCFV displaying transitional values. Previous studies indicate

that carbonate precipitated from high-temperature burial or hydrothermal fluids typically exhibits depleted $\delta^{18}O$ values, generally below −10‰ [28]. The consistently negative $\delta^{18}O$ values observed in calcite from the BCFV, as well as calcite and northupite from the Y-HFV, strongly suggest a high-temperature deep-seated fluid origin. Furthermore, because carbon isotope fractionation in carbonates is highly sensitive to organic matter incorporation [29,30], the significantly lower $\delta^{13}C$ values compared to contemporaneous seawater [31,32] indicate that these upward-migrating hydrothermal fluids efficiently incorporated ^{12}C-enriched organic carbon from the surrounding alkaline shale during metasomatism [23,33].

Strontium isotopes provide further critical constraints on fluid sources, though their interpretation requires careful evaluation of potential crustal contamination. In Figure 9 (with analytical uncertainties indicated by error bars), the $^{87}Sr/^{86}Sr$ ratios of vein-filling minerals are substantially lower than the average value of the Permian continental crust (0.71600; [34]) and fall outside the global Permian seawater/carbonate range (0.70740–0.70815; [35]). While the measured ratios (0.70487–0.70574) broadly overlap with the mantle-derived Permian Sr isotopic range (0.70350–0.70582; [27]), directly attributing these to pure mantle-exsolved fluids in a sedimentary basin context oversimplifies the geological reality. Due to the lack of Sr concentration data, a rigorous quantitative mixing-line calculation cannot be performed; however, a qualitative assessment of fluid mixing can be robustly established using geological context and isotopic trends.

The Mahu Sag basement and underlying strata feature extensive Permian volcanic rocks, which inherently possess low, mantle-like $^{87}Sr/^{86}Sr$ signatures. We interpret that deep basinal hydrothermal fluids likely interacted extensively with this volcanic basement, leaching Sr and thereby inheriting its low $^{87}Sr/^{86}Sr$ fingerprint. Notably, the upper limit of the measured vein ratios (up to 0.70574) is systematically and slightly elevated compared to typical unaltered Permian mantle/basaltic values (usually <0.7050). This subtle isotopic shift, combined with the highly negative $\delta^{13}C$ values observed in the C-O isotopes, provides strong qualitative evidence against an unmixed mantle source. Instead, it indicates that during their upward migration, these deep, volcanically influenced hydrothermal fluids underwent measurable mixing with higher-$^{87}Sr/^{86}Sr$ fluids—most likely contemporaneous alkaline lacustrine pore waters or residual Permian–Triassic seawater—and simultaneously interacted with organic-rich shale. Therefore, we refine our interpretation: the vein fillings were derived from deep-seated hydrothermal fluids that inherited a mantle-like Sr signature via basement interaction, which were subsequently contaminated by sedimentary formation fluids during upward migration.

5.1.2. Growth Mechanisms of Bedding-Complex Fracture Veins

The development of bedding-parallel fractures is primarily governed by fluid overpressure. Tensile fracturing initiates when the pore fluid pressure exceeds the critical threshold defined by the sum of overburden pressure and shale tensile strength, thereby disrupting the rock's stress equilibrium [36]. During tensile fracturing, displacement vectors across the fracture walls are oriented approximately perpendicular to the bedding planes. Following fracture opening, externally derived fluids infiltrate the fracture system. As the fluid pressure decreases, the solubility of dissolved solutes declines, inducing fluid supersaturation and triggering mineral precipitation. Organic acid dissolution, lake water alkalinization, and late-stage hydrothermal overprinting collectively facilitated fracture sealing, reactivation, and the precipitation of three-stage mineral assemblages (quartz, calcite, and dolomite).

Quartz veins exhibit the most extensive distribution, with unaltered quartz grains retained within the interstices of calcite and dolomite. Therefore, it can be inferred that

the primary spatial framework of the bedding-parallel complex fracture veins was established during the quartz vein generation period. Hydrocarbon generation provided the fundamental driving force for this process [37]. Hydrocarbon–water–rock interactions supplied the carbon sources and fluids for vein formation, while the generated petroleum and natural gas induced overpressure, opening the bedding-parallel fractures and creating accommodation space. This overpressure-driven mechanism is recognized as the primary growth mechanism for quartz and calcite veins, a conclusion strongly corroborated by the distribution characteristics of oil and bitumen inclusions. Additionally, the peak homogenization temperatures of fluid inclusions in quartz, calcite, and dolomite are 58.6 °C, 67.4 °C, and 84.4 °C, respectively, reflecting a progressive increase in formation temperature concomitant with greater burial depth.

Following quartz vein formation, fluid salinity within the veins increased abruptly, indicating intensified lake water salinization and enhanced hydrothermal activity at the lake bottom. Concurrently, external formation fluids delivered Mg^{2+}-enriched solutions. As indicated by the carbon and oxygen isotope signatures, these fluids were partially derived from Permian–Triassic boundary seawater sources. These conditions facilitated extensive dolomitization, whereby dolomite replaced pre-existing calcite veins and occupied the remaining fracture spaces.

Furthermore, the dominant reverse faulting stress regime in this area provides a favorable macro-mechanical context for the development of these bedding-parallel fractures. 3D in situ stress simulations of the Fengcheng Formation indicate that the study area is dominated by horizontal stress, with the maximum horizontal principal stress oriented northeastward, and the stress regime is primarily thrust-dominated [38]. Under this specific thrust fault stress regime, the vertical stress acts as the minimum principal stress. Consequently, when the fluid overpressure exceeds the tensile strength, the rock is most prone to developing horizontal tensile fractures parallel to the bedding. This mechanical reality is highly consistent with the mechanism of the BCFV opening along bedding planes, indicating that the late-stage tectonic stress field macroscopically controlled and enhanced the fluid overpressure-dominated bedding-parallel fracturing process by creating a highly favorable stress state.

5.1.3. Growth Mechanisms of Y-HFV

While tectonic stress is conventionally regarded as the primary driver for high-angle fracture opening, the discovery of "Y"-shaped high-angle fracture veins (Y-HFVs) in this study suggests a more complex genesis in alkaline lake depositional settings, where fluid–mineral interactions significantly contribute to the fracturing process. This multi-stage evolution is closely related to multiple phases of tectonic inversion and strike–slip activity in the Mahu Sag since the Late Permian. Regional tectonic analysis indicates that a series of right-lateral strike–slip fault systems (e.g., Ke-Bai and Wu-Xia Fault Zones) developed along the northwestern margin of the Junggar Basin, experiencing critical activity during the Late Permian and Late Triassic [39]. The Late Permian tectonic inversion transformed the early rift basin configuration and triggered initial compressive deformation, while Late Triassic reactivation essentially shaped the present-day mountain–basin configuration. These two phases of tectonic activity provided a continuous source of stress for the opening and modification of high-angle fractures (Figure 16).

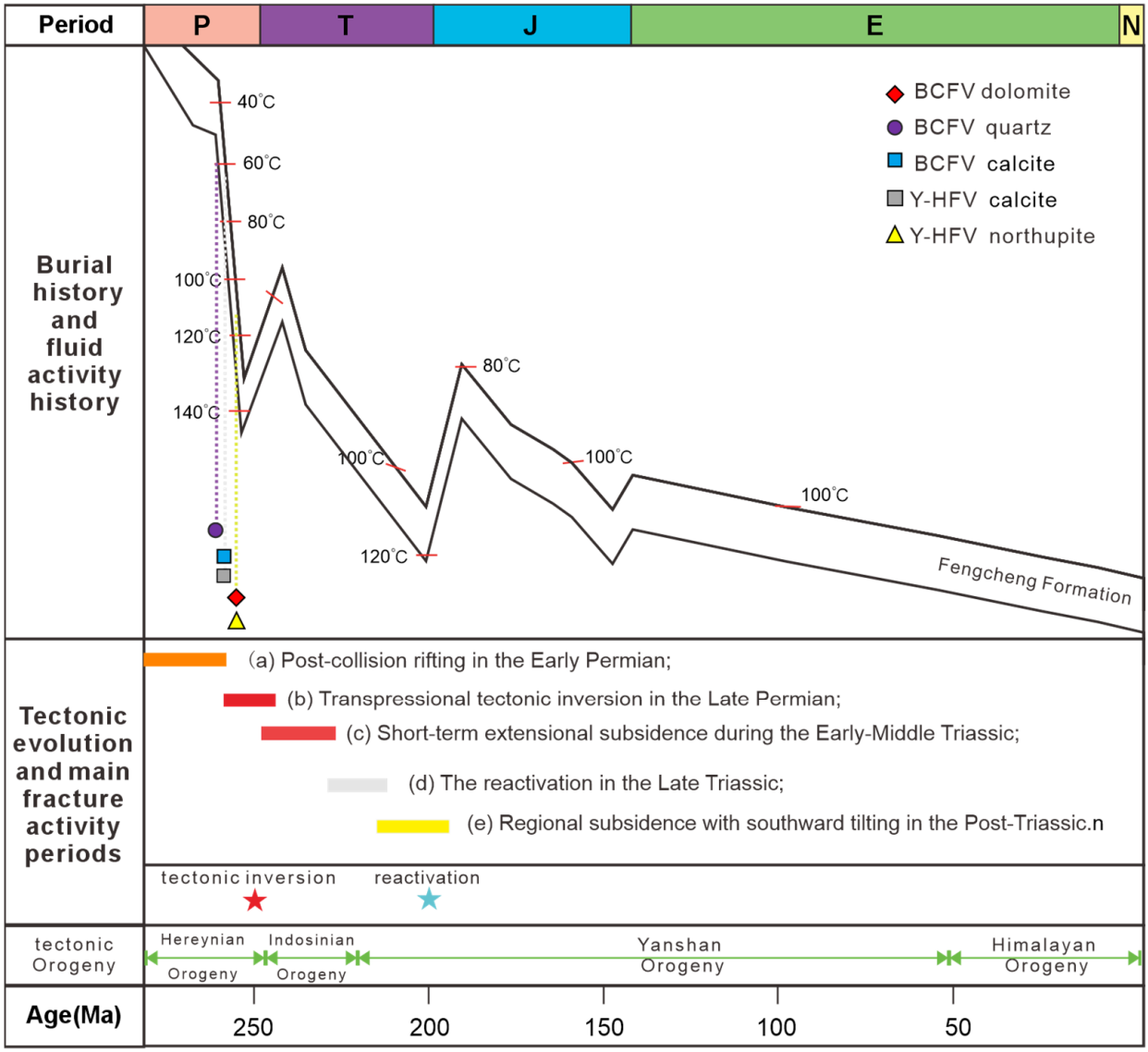


Figure 16. Fluid evolution and tectonic history of Fengcheng Formation in Ma Hu depression. Burial history modified from [33,40]; tectonic evolution-related information extracted from [39].

The formation of initial pores and fractures was driven by evaporative concentration-induced rock embrittlement and overpressure fracturing from organic matter thermal maturation. Following initial hydrocarbon charging, subsequent tectonic stress modified the fracture system, causing adjacent wall rocks to undergo shear displacement, with fracture propagation deviating from a near-vertical orientation to follow the tectonic stress trajectory [41]. Subsequently, precipitation from mixed exotic and indigenous formation fluids formed northupite vein-filling minerals. pH fluctuations triggered dissolution–reprecipitation cycles of alkaline minerals, which—superimposed on lacustrine hydrothermal activities—drove fracture annealing and reactivation processes, predominantly generating calcite veins.

The highly variable cathodoluminescence colors in the Y-HFV indicate an exceptionally complex fluid alteration history. Integrated CL, petrographic characteristics, and homogenization temperature data reveal that early-formed calcite was distributed along dissolution pores and fractures. As the alkaline lake water evolved, northupite precipitated, partially filling spaces created by calcite dissolution. Because the lake water repeatedly fluctuated between acidic and alkaline conditions, both vein types underwent multiple

stages of alteration, jointly filling the "Y"-shaped space. Notably, some veins exhibit a fibrous stretching morphology. Nearby fluid inclusions are observed to be stretched laterally toward the country rock under transverse stress (Figure 14a). This stretching direction opposes the tectonic stress and is likely associated with overpressure fracturing caused by the continuous thermal evolution of organic matter.

Fracture development in alkaline lake shale is governed by a multifactor control mechanism: tectonic stress and overpressure drive fracture propagation, while alkaline fluids continuously modify fracture and pore structures. Based on the morphological characteristics of calcite and northupite, it can be inferred that the subsequent formation of northupite and its replacement of calcite drove the upward propagation of the original fractures. The unique chemical properties of alkaline fluids and specific alkaline minerals can induce directional fracture propagation, alter fracture angles, and ultimately govern the aperture width and final morphology of the fractures.

The propagation direction of the observed Y-HFV is directly controlled by the aforementioned strike–slip–compression stress field. In situ stress measurements show that the current maximum horizontal principal stress in the study area is oriented northeast (~28°) [38], broadly parallel to the strike of the regional strike–slip fault zones. Under a right-lateral strike–slip tectonic setting, the derived local compressive stress field likely dominated the development of high-angle shear fractures in a northwest–southeast direction (or oblique to it). Therefore, the formation of the Y-HFV can be regarded as a composite product: after initial micro-fractures were generated by hydrocarbon generation, the fractures were activated, opened, and subjected to shear displacement under the continuous regional strike–slip–compression stress field from the Late Permian to the Late Triassic, and were subsequently modified by alkaline fluids. The tectonic stress field not only controls the occurrence and network pattern of the fractures but also provides preferential pathways for later fluid migration and mineral precipitation.

5.2. Dynamic Evolution Model of Shale Fracture Veins in Alkaline Lake Environment

5.2.1. Differences in the Development Environments of Different Fracture Veins in Alkaline Lacustrine Shales

The sedimentary processes in alkaline lake environments are remarkably complex. Observations from the Fengcheng Formation in the Maye-1 and Fengcheng-1 wells reveal two distinct fracture vein types where the distribution and development of characteristic alkaline minerals (northupite, shortite, reedmergnerite, etc.) differ dramatically not only between the veins themselves but also within their respective host rocks.

In the BCFV of Well Maye-1, the reedmergnerite content is limited to only 0.53%, occurring predominantly within the mudstone matrix where it coexists with pyrite. The pyrite content here is significantly higher (4.45%) and occurs mainly in nodular forms. Conversely, in the Y-HFV of Well Fengcheng-1, the pyrite content reaches 5.55%, occurring predominantly as bedding-parallel bands with minor nodular forms. This specific mineral assemblage suggests intensified localized reducing conditions and/or an enrichment of iron and organic matter during sedimentary or early diagenetic processes [42]. It is therefore inferred that weakly alkaline conditions prevailed in the Fengcheng Formation during the initial fracturing stage, accompanied by intense hydrocarbon generation from organic matter [43]. The formation of pyrite in these mudstones is predominantly linked to microbe-mediated sulfate reduction within anoxic environments [44].

As the alkaline lake sediments evolved, alkalinity intensified within the stratigraphic sequence, leading to localized enrichment of alkaline minerals. This is exemplified by the significantly elevated northupite content in the Y-HFV of Well Fengcheng-1, indicating a shift toward enhanced alkaline conditions dominated by sodium carbonate evaporite deposition [41].

5.2.2. Dynamic Evolution of BCFV in Alkaline Lacustrine Shales

The infilling process of bedding-parallel fracture veins typically involves two stages: initial fracture opening followed by the accelerated crystallization of fibrous minerals. This process is intrinsically linked to anomalous fluid pressures, a mechanism well-documented in other basins; for instance, vein formation in the Longmaxi Formation shale of the Sichuan Basin correlates with overpressured fluid activities induced by the Indosinian tectonic event during the Middle–Late Triassic [45].

The evolutionary sequence of bedding-parallel composite fracture veins in the Well Maye-1 area comprises four distinct stages (Figure 17):

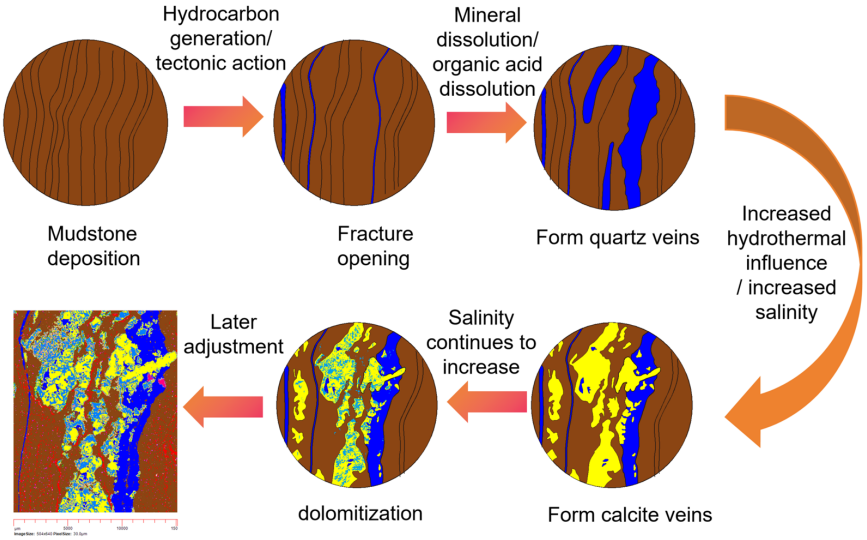


Figure 17. BCFV growth process dynamic model.

Stage 1 (Quartz Vein Formation): Hydrocarbon enrichment generates overpressure, promoting fracture opening. Initial fractures form, enabling hydrocarbon migration from micro-fractures into dilated fractures. These hydrocarbons subsequently mix with exogenous fluids to infill the fractures, precipitating the first-stage quartz veins.

Stage 2 (Calcite Vein Formation): Secondary fluids, derived from lake water evaporation and alkaline hydrothermal activity, infiltrate the fracture system. This facilitates calcite precipitation, which progressively infills the remaining fracture space.

Stage 3 (Dolomite Vein Formation): As homogenization temperatures and fluid salinities increase concurrently with the influx of Mg-rich external fluids, the pre-existing calcite veins undergo extensive dolomitization, ultimately transforming into dolomite veins.

Stage 4 (Composite Vein Alteration): Fluid re-equilibration, driven by changing formation temperatures and pressures, triggers mineral exchange between the veins and the host rock. This results in the formation of composite assemblages, such as alstonite–quartz and pyrite–calcite mixtures.

5.2.3. Dynamic Evolution of Y-HFV in Alkaline Lacustrine Shales

The infilling process of the Y-HFV exhibits considerable complexity, with its morphology evolving throughout the mineralization sequence. This stands in stark contrast to BCFV development, which primarily preserves the initial fracture orientation. Under the combined influence of tectonic forces and dissolution processes, the overall configuration and aperture angle of the Y-HFV continuously adjust. These dynamic modifications are further facilitated by pH fluctuations within the alkaline fluids.

The evolutionary sequence of the Y-HFV unfolds as follows (Figure 18): Initially, micro-fractures develop under the effects of hydrocarbon generation overpressure. These

micro-fractures establish effective permeability by interconnecting previously isolated micropores within the shale reservoir, creating an integrated pore network. Subsequent regional tectonic stress induces the formation of steeply dipping fractures. Following this, the injection of later-stage alkaline fluids further enlarges the pore spaces while facilitating mineral replacement and elemental exchange with the host rock.

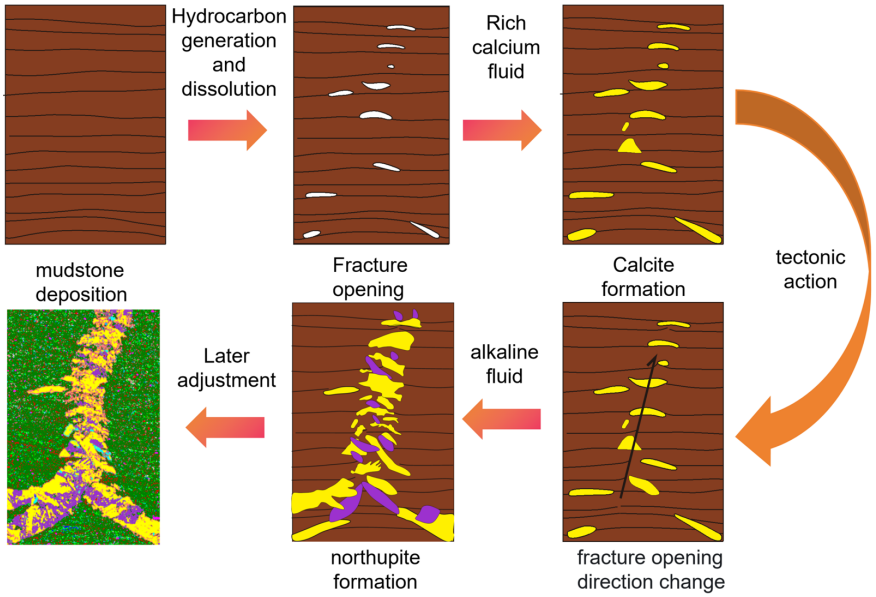


Figure 18. Y-HFV growth process dynamic model.

Crucially, the repeated dissolution of early calcite and reprecipitation of alkaline minerals (like northupite) remodel the fractures into irregular veins. This fluid–mineral interaction, combined with ongoing tectonic shear, causes fractures to coalesce and propagate upward, ultimately forming the characteristic "Y"-shaped geometry. The entire sequence is governed by the synergistic interplay of alkaline mineralization, tectonic stress, and fluid dynamics, highlighting that in alkaline lacustrine shales, fracture morphology is as much a product of geochemical alteration as it is of mechanical stress.

5.2.4. Limitations of Dynamic Evolution Model of Shale Fracture Veins

While the samples utilized in this study are limited to two wells (Maye 1 and Fengcheng 1) and targeted thin sections, they are considered typical representatives of the Fengcheng Formation shale in the northern slope zone of the Mahu Sag. The two wells are strategically located at different structural positions within the sag, capturing the primary fracture development characteristics of the region. To provide quantitative justification for this representation, a systematic core observation was conducted over a total length of 184.9 m (88.6 m in Maye 1 Well and 96.3 m in Fengcheng 1 Well). Within this interval, 16 major sets of multi-stage fracture veins were identified, specifically comprising 11 sets of BCFVs (with dip angles ranging from 5° to 25°) and five sets of Y-HFVs (with dip angles ranging from 75° to 90°). It is acknowledged that aside from these multi-stage veins, single-stage bedding-parallel fractures and high-angle fractures are also present in the cores. However, since these single-stage fractures have been extensively observed and documented in the previous literature [46–48], this study specifically focuses on the more complex, multi-stage vein systems.

Despite these quantitative justifications, a fundamental limitation of this study must be explicitly acknowledged. The fluid evolution and dynamic fracture models derived from detailed analyses of these specific thin sections represent a localized, albeit highly detailed, conceptual model rather than a regionally averaged statistic. The spatial coverage

remains inherently restricted by the number of available wells and samples. Consequently, while the proposed "alkaline minerals–stress–fluids" synergistic mechanism provides a robust microscopic explanation for the studied intervals, its direct extrapolation across the entire Mahu Sag requires caution. Future work should prioritize expanding the sampling density across the northern slope zone. Integrating additional drilling cores and systematic analyses from newly drilled wells will be essential to verify the regional applicability of the dynamic evolution model proposed in this study.

5.3. The Evolution Process of Hydrocarbons in Fracture Veins

5.3.1. Hydrocarbon Evolution in BCFV

During the early burial stages, as depth and temperature increased, the organic-rich Fengcheng Formation source rocks in the Mahu Sag reached the hydrocarbon generation threshold by the Late Permian, initiating the expulsion of immature hydrocarbons [49]. A portion of these generated hydrocarbons was adsorbed onto mineral surfaces, while the free phase was expelled into pore spaces [37]. Continuous subsidence intensified rock anisotropy and pore fluid pressure buildup, facilitating the development of bedding-parallel fractures [48].

Hydrocarbons progressively migrated from the shale matrix into early-stage microfractures, generating local overpressure that promoted fracture propagation. As these microfractures dilated, they mixed with exogenous fluids, precipitating the first-stage quartz veins while trapping early, low-maturity hydrocarbon inclusions. Organic acids generated during this process further enlarged the fractures, providing additional accommodation space. Subsequently, the infiltration of secondary fluids led to the precipitation of calcite veins, which incorporated migrating hydrocarbons into their growth zones.

Crucially, as burial continued, the early hydrocarbons entrapped within the quartz veins underwent intense thermal cracking. The vapor–liquid–solid multiphase assemblages observed in quartz—comprising liquid hydrocarbons, gaseous hydrocarbons, and solid bitumen—represent direct evidence of this cracking process. In contrast, calcite veins exclusively preserve unaltered, immature hydrocarbon inclusions (yellow-green fluorescence), indicating that hydrocarbons charging into the fractures at this intermediate stage escaped extensive thermal decomposition. Finally, the third-stage dolomite veins exhibit a drastic reduction in hydrocarbon inclusion abundance, dominated instead by non-luminescent gas inclusions. This signifies the cessation of the peak liquid hydrocarbon generation window in the shale during the late-stage fluid influx.

5.3.2. Hydrocarbon Evolution in Y-HFV

Similar to the BCFV, hydrocarbon generation and dissolution jointly drove the formation of primary pore–fracture networks in the Y-HFV, which were subsequently expanded and connected by tectonic stress. This process sequentially precipitated calcite veins followed by northupite veins, accompanied by continuous hydrocarbon charging.

Despite Well Fengcheng-1 (Y-HFV) and Well Maye-1 (BCFV) targeting identical stratigraphic units with shared source rock origins [49], the hydrocarbon evolution profiles in the Y-HFV are distinctly different. Although Well Fengcheng-1 is located at a structural high—which typically suggests earlier hydrocarbon charging and higher thermal maturity—the fluid inclusions here exhibit anomalously lower maturity. Calcite veins in the Y-HFV contain a mixture of blue-white (higher maturity) and yellow-green (lower maturity) fluorescent liquid hydrocarbon inclusions. More notably, the extensively developed northupite veins host inclusions that appear light brown under transmitted light and display significantly lower-maturity fluorescence under UV excitation. Adjacent bitumen inclusions within the northupite likely represent early-stage asphaltene precipitation. This

unambiguous fluorescence contrast confirms the exceptional preservation of low-maturity hydrocarbons migrated from the shale into the Y-HFV system, distinctly different from the extensive cracking observed in the BCFV.

5.3.3. Implications of Hydrocarbon Evolution in Shale Fracture Veins

The thermal maturation of organic matter is not solely controlled by temperature and burial history; it is also profoundly influenced by the local geochemical environment, particularly pH, salinity, and organic–inorganic interactions [50,51]. Recent experimental studies demonstrate that alkaline minerals can suppress organic matter maturation, enhance total organic carbon (TOC) conversion rates, and delay the peak oil generation window via "saponification reactions" [18].

This theoretical framework provides a compelling explanation for the contrasting hydrocarbon inclusion characteristics observed between the two fracture types in this study. The BCFV, which generally exhibits low alkaline mineral content, records an uninterrupted thermal evolution: early-charged hydrocarbons were thoroughly cracked into high-maturity blue-green/pale blue fluorescent products and solid bitumen. Conversely, the Y-HFV is characterized by abundant alkaline minerals (notably northupite) and fluid inclusions with significantly higher salinity. In this system, the synergistic effects of alkaline minerals and high-salinity/pH fluids formed a local "geochemical barrier." This barrier effectively retarded the in situ thermal cracking of hydrocarbons. Consequently, the migrating hydrocarbons were "frozen" in a low-maturity state (preserving yellow-green fluorescence and light brown colors), completely avoiding the extensive thermal decomposition seen in the BCFV. Therefore, we propose that in alkaline lacustrine shale systems, the higher the alkaline mineral content and fluid salinity within fracture vein assemblages, the stronger the inhibitory effect on hydrocarbon maturation, ultimately leading to differential hydrocarbon preservation potentials (Figure 19).

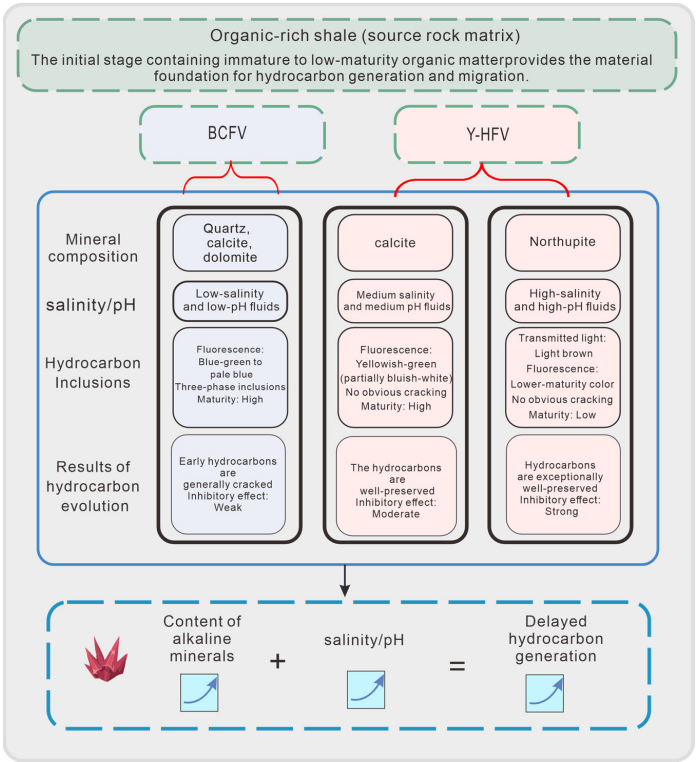


Figure 19. Schematic diagram illustrating interrelationships among controlling factors of hydrocarbon evolution.

6. Conclusions

(1) Fracture networks serve as critical pathways for efficient shale oil migration and enrichment. Their multi-stage opening in alkaline lacustrine shales is fundamentally governed by the synergistic interplay of "alkaline minerals–stress–fluids", where tectonic stress and overpressure drive fracture propagation, and subsequent alkaline fluids remodel fracture and pore structures.

(2) Despite different evolutionary paths, both vein types experienced initial hydrocarbon charging during comparable timeframes. The BCFV underwent three distinct fluid modification events and multi-phase growth driven by fluid evolution and hydrocarbon charging. In contrast, the Y-HFVs evolved sequentially from hydrocarbon generation micro-fractures to tectonic-driven high-angle fractures, and were ultimately remodeled into vertically bedding-transgressive veins by alkaline fluid influx. Carbon–oxygen–strontium isotopes and fluid inclusion temperatures confirm this synchronized initial charging.

(3) Post-charging fluid behaviors diverged significantly. BCFVs in organic-rich shales contain lower alkaline minerals but higher-maturity inclusions, where early-charged hydrocarbons commonly underwent cracking. Conversely, Y-HFVs display a higher alkaline mineral content and lower inclusion maturity, effectively preserving migrated hydrocarbons without significant cracking.

(4) Most notably, vein assemblages containing alkaline minerals exert a remarkable inhibitory effect on the maturity evolution of entrapped hydrocarbon inclusions. The intensity of this inhibition increases in a dose-dependent manner with higher fluid salinity and pH levels.

Author Contributions: Conceptualization, K.L.; Methodology, J.H.; Formal analysis, K.L.; Investigation, J.H.; Resources, Z.H., G.Z.; Software, Z.H., J.F.; Validation, J.L., H.G.; Writing—original draft, K.L.; Writing—review & editing, G.Z.; Funding acquisition, G.Z. All authors have read and agreed to the published version of the manuscript.

Funding: This research was funded by National Natural Science Foundation of China Project (No. 42302154; No. 42272142).

Data Availability Statement: The data that support the findings of this study are available from the corresponding author upon reasonable request.

Acknowledgments: The authors thank the three anonymous reviewers for their constructive comments and suggestions, which significantly improved the initial manuscript, as well as the Assistant Editor and Academic Editor for their editorial handling.

Conflicts of Interest: The authors declare no conflicts of interest. Jiakai Hou, Zhenkai Huang and Jiangna Fu are employed by Research Institute of Petroleum Exploration and Development, PetroChina. The paper reflects the views of the scientists and not the companies.

References

1. Gong, L.; Wang, J.; Gao, S.; Fu, X.; Liu, B.; Miao, F.; Zhou, X.; Meng, Q. Characterization, controlling factors and evolution of fracture effectiveness in shale oil reservoirs. *J. Pet. Sci. Eng.* **2021**, *203*, 108655. [CrossRef]
2. Hou, D.; Cheng, X.; Wei, L.; Li, Y.; Li, K.; Zhang, Z.; Zhang, H.; Bian, J.; Li, Y.; Si, W.; et al. Oil and natural gas geochemistry in offshore China: Advances and challenges. *Nat. Gas Ind. B* **2024**, *11*, 631–644. [CrossRef]
3. Shen, W.; Ma, T.; Zuo, L.; Yang, X.; Cai, J. Advances and Prospects of Supercritical CO_2 for Shale Gas Extraction and Geological Sequestration in Gas Shale Reservoirs. *Energy Fuels* **2024**, *38*, 789–805. [CrossRef]
4. Sheng, C.; Yuan, L.; Jiao, J.J.; Cai, P.; Luo, X.; Zuo, J.; Xiao, K.; Hensen, C. Multimillennial climate-freshwater legacy beneath a large-river delta-front estuary. *Sci. Adv.* **2026**, *12*, eaeb6352. [CrossRef]
5. Zhu, H.; Ju, Y.; Lu, Y.; Yang, M.; Feng, H.; Qiao, P.; Qi, Y. Natural evidence of organic nanostructure transformation of shale during bedding-parallel slip. *Geol. Soc. Am. Bull.* **2025**, *137*, 2719–2746. [CrossRef]

6. Ali, J.; Ansari, U.; Ali, F.; Javed, T.; Hullio, I.A. Application of Machine Learning for Effective Screening of Enhanced Oil Recovery Methods. *Reserv. Sci.* **2026**, *2*, 65–80. [CrossRef]
7. Chogani, A.; King, H.E.; Tutolo, B.; Živković, A.; Plümper, O. Geochemistry of lithospheric aqueous fluids modified by nanoconfinement. *Nat. Geosci.* **2025**, *18*, 191–196. [CrossRef]
8. Khan, M.; Nawaz, S.; Gao, X.; Khan, N.M. Reservoir Characterization of Eocene Carbonates and Cambrian Sands in the Eastern Potwar Region, Pakistan. *Reserv. Sci.* **2026**, *2*, 111–125. [CrossRef]
9. Trail, D.; McCollom, T.M. Relatively oxidized fluids fed Earth's earliest hydrothermal systems. *Science* **2023**, *379*, 582–586. [CrossRef]
10. Tian, L.; Zhang, Q.; Li, X.; Li, C. Fracturing Effectiveness Evaluation Based on Flowback Data Using Pressure Transient Testing. *Reserv. Sci.* **2026**, *2*, 97–110. [CrossRef]
11. Hu, Y.; Yang, Y. A Comparative Study on Drag Reduction Methods for Continental Shale Drilling in the Fuxing Block, Southeastern Sichuan Basin. *Reserv. Sci.* **2026**, *2*, 81–96. [CrossRef]
12. Yang, M.; Pan, Y.; Feng, H.; Yan, Q.; Lu, Y.; Wang, W.; Qi, Y.; Zhu, H. Fractal Characteristics of Pore Structure of Longmaxi Shales with Different Burial Depths in Southern Sichuan and Its Geological Significance. *Fractal Fract.* **2025**, *9*, 2. [CrossRef]
13. Li, Y.; Feng, Z.; Zhang, Q.; Xu, S.; Wang, W.; Li, H.; Zhou, S. Multifractal characteristics of nanopores in the Zhaotong national shale gas demonstration area, Southern Sichuan Basin, China. *Nat. Gas Ind. B* **2025**, *12*, 647–661. [CrossRef]
14. Tan, R.; Wang, R.; Huang, Y.; Yang, R.; Li, H.; Lu, K. Mechanism of the Enrichment and Loss Progress of Deep Shale Gas: Evidence from Fracture Veins of the Wufeng–Longmaxi Formations in the Southern Sichuan Basin. *Minerals* **2022**, *12*, 897. [CrossRef]
15. Sun, C.; Nie, H.; Liu, G.; Zhang, G.; Du, W.; Wang, R. Controls of quartz mineral types on the enrichment and exploitation of shale gas: A case study of the Wufeng-Longmaxi Formations in the Sichuan Basin and its periphery. *Earth Sci.* **2019**, *44*, 3692–3704. [CrossRef]
16. Tang, Y.; Jia, C.; Chen, F.; He, W.; Zhi, D.; Shan, X.; You, X.; Jiang, L.; Zou, Y.; Wu, T.; et al. Relationship between pore throat structure and crude oil mobility of full particle sequence reservoirs in Permian Fengcheng Formation, Mahu Sag, Junggar Basin, NW China. *Pet. Explor. Dev.* **2025**, *52*, 112–124. [CrossRef]
17. Cao, J.; Xia, L.; Wang, T.; Zhi, D.; Tang, Y.; Li, W. An alkaline lake in the Late Paleozoic Ice Age (LPIA): A review and new insights into paleoenvironment and petroleum geology. *Earth-Sci. Rev.* **2020**, *202*, 103091. [CrossRef]
18. Cao, J.; Zhang, R.; Zhi, D.; Tang, Y.; Xia, L.; He, W. Unique bimodal oil generation of alkaline-saline lacustrine source rock: Evidences, model and mechanism of organic-inorganic interactions. *Sci. China Earth Sci.* **2025**, *68*, 1559–1582. [CrossRef]
19. Liu, D.; Wu, J.; Zhao, S.; Tang, X.; Zhang, D.; Wang, Q.; Huang, S.; Zhang, C.; Tan, P. Experimental study on hydraulic fracture propagation in middle-deep shale gas reservoirs in the southern Sichuan Basin: The effects of vertical heterogeneity. *Nat. Gas Ind. B* **2025**, *12*, 705–717. [CrossRef]
20. Zhang, Y.; Zeng, L.; Luo, Q.; Zhu, R.; Pan, S.; Dai, Q.; Shi, J.; Qin, J.; Xu, X. Effects of diagenesis on natural fractures in tight oil reservoirs: A case study of the Permian Lucaogou Formation in Jimusar Sag, Junggar Basin, NW China. *Geol. J.* **2020**, *55*, 6562–6579. [CrossRef]
21. Ni, M.; Zhang, Y.; Tang, Y.; He, W. Distribution characteristics of organic matter in the Fengcheng Formation in Mahu Sag, Junggar Basin: Implications for hydrocarbon generation model in alkaline lacustrine deposition. *Front. Earth Sci.* **2023**, *11*, 1218788. [CrossRef]
22. Zhang, Y.; Li, W.; Tang, W. Tectonic setting and formation environment of alkaline lacustrine source rocks of the Fengcheng Formation in the Mahu Sag. *Xinjiang Pet. Geol.* **2018**, *39*, 1. [CrossRef]
23. Huang, H.; Chen, H.; Huo, F.; Yang, S.; Chen, A. Effects of Deep Fluids on Middle Permian Dolomite of the Western Sichuan Basin. *Front. Earth Sci.* **2022**, *10*, 910453. [CrossRef]
24. He, D.; Wu, S.; Zhao, L.; Zheng, M.; Li, D.; Lu, Y. Sedimentary and tectonic setting and evolution of the Permian-Triassic system around the Mahu Sag. *Xinjiang Pet. Geol.* **2018**, *39*, 1. [CrossRef]
25. Tang, Y.; Zheng, M.; Wang, X.; Wang, T.; Xie, Z.; Qin, Z.; Hei, C.; Cheng, H.; Gao, Y.; Tao, H. Sedimentary paleoenvironment of source rocks of the Fengcheng Formation in the Mahu Sag, Junggar Basin. *Nat. Gas Geosci.* **2022**, *33*, 677–692. [CrossRef]
26. Bodnar, R.J. Revised equation and table for determining the freezing point depression of H_2O-NaCl solutions—ScienceDirect. *Geochim. Cosmochim. Acta* **1993**, *57*, 683–684. [CrossRef]
27. Veizer, J.; Ala, D.; Azmy, K.; Bruckschen, P.; Buhl, D.; Bruhn, F.; Carden, G.A.F.; Diener, A.; Ebneth, S.; Godderis, Y.; et al. 87Sr/86Sr, δ13C and δ18O evolution of Phanerozoic seawater. *Chem. Geol.* **1999**, *161*, 59–88. [CrossRef]
28. Montaez, I.P.; Banner, J.L.; Osleger, D.A.; Borg, L.E.; Bosserman, P.J. Integrated Sr isotope variations and sea-level history of Middle to Upper Cambrian platform carbonates: Implications for the evolution of Cambrian seawater 87Sr/86Sr. *Geology* **2015**, *24*, 917–920. [CrossRef]
29. Berner, R.A. Sedimentary pyrite formation: An update. *Geochim. Cosmochim. Acta* **1984**, *48*, 605–615. [CrossRef]
30. Grotzinger, J.P.; Knoll, A.H. Stromatolites in Precambrian Carbonates: Evolutionary Mileposts or Environmental Dipsticks? *Annu. Rev. Earth Planet. Sci.* **1999**, *27*, 313–358. [CrossRef] [PubMed]

31. Holmes, K.M. Using Pliocene palaeoclimatic data to postulate dispersal pathways of early hominins. *Palaeogeogr. Palaeoclimatol. Palaeoecol.* **2007**, *248*, 96–108. [CrossRef]
32. Korte, C.; Kozur, H.W. Carbon-isotope stratigraphy across the Permian–Triassic boundary: A review. *J. Asian Earth Sci.* **2010**, *39*, 215–235. [CrossRef]
33. Wang, W.; Xie, X.; Liu, C.; Cao, F.; Zheng, G.; Wang, Z.; Chen, G.; Deng, H.; He, J.; Li, K. Characteristics and Formation Stages of Natural Fractures in the Fengcheng Formation of the Mahu Sag, China: Insights from Stable Carbon and Oxygen Isotope and Fluid Inclusion Analysis. *Minerals* **2023**, *13*, 894. [CrossRef]
34. Rudnick, R.L.; Gao, S. 4.1—Composition of the Continental Crust. In *Treatise on Geochemistry*, 2nd ed.; Holland, H.D., Turekian, K.K., Eds.; Elsevier: Oxford, UK, 2014; pp. 1–51.
35. Veizer, J.; Compston, W. 87Sr/86Sr composition of seawater during the Phanerozoic. *Geochim. Cosmochim. Acta* **1974**, *38*, 1461–1484. [CrossRef]
36. Du, X.-Y.; Jin, Z.-J.; Zeng, L.-B.; Liu, G.-P.; Li, S.-X.; Ostadhassan, M.; Liang, X.-P.; Wang, G.-P.; Lu, G.-Q. Characteristics, controlling factors and mechanisms of natural fractures formation in lacustrine shale oil reservoirs: The Chang 7 member in Ordos Basin, China. *Pet. Sci.* **2025**, *22*, 1391–1406. [CrossRef]
37. Hunt, J.M. Generation and migration of petroleum from abnormally pressured fluid compartments. *AAPG Bull.* **1990**, *74*, 1–12. [CrossRef]
38. Chen, P.; Qiu, H.; Chen, X.; Shen, C. Refined 3D Numerical Simulation of In Situ Stress in Shale Reservoirs: Northern Mahu Sag, Junggar Basin, Northwest China. *Appl. Sci.* **2024**, *14*, 7644. [CrossRef]
39. Tian, X.; Zhang, Y.; Zhuo, Q.; Yu, Z.; Guo, Z. Charging characteristics of tight oil in the Lower Permian Fengcheng Formation, Mahu Sag, Junggar Basin: Evidence from fluid inclusions in alkaline minerals. *Acta Pet. Sin.* **2019**, *40*, 646–659. [CrossRef]
40. Liang, Y.; Zhang, Y.; Chen, S.; Guo, Z.; Tang, W. Controls of a strike-slip fault system on the tectonic inversion of the Mahu depression at the northwestern margin of the Junggar Basin, NW China. *J. Asian Earth Sci.* **2020**, *198*, 104229. [CrossRef]
41. Yu, K.; Cao, Y.; Qiu, L.; Sun, P. Depositional environments in an arid, closed basin and their implications for oil and gas exploration: The lower Permian Fengcheng Formation in the Junggar Basin, China. *AAPG Bull.* **2019**, *103*, 2073–2115. [CrossRef]
42. Wang, T.; Cao, J.; Carroll, A.R.; Zhi, D.; Tang, Y.; Wang, X.; Li, Y. Oldest preserved sodium carbonate evaporite: Late Paleozoic Fengcheng Formation, Junggar Basin, NW China. *GSA Bull.* **2020**, *133*, 1465–1482. [CrossRef]
43. Ni, M.; Zhu, H.; He, W.; Yang, S.; Zou, Y.; Zhang, Y. Analysis of sedimentary environment and sedimentary model of the Fengcheng Formation in the Mahu Sag, Junggar Basin. *Geoscience* **2023**, *37*, 1194–1207. [CrossRef]
44. Berner, R.A. Sedimentary pyrite formation. *Am. J. Sci.* **1970**, *268*, 1–23. [CrossRef]
45. Liang, C.; Jiang, Z.; Yang, Y.; Wei, X. Shale lithofacies and reservoir space of the Wufeng–Longmaxi Formation, Sichuan Basin, China. *Pet. Explor. Dev.* **2012**, *39*, 736–743. [CrossRef]
46. Wang, S.; Wang, G.; Zeng, L.; Liu, P.; Huang, Y.; Li, S.; Wang, Z.; Zhou, Y. New method for logging identification of natural fractures in shale reservoirs: The Fengcheng formation of the Mahu Sag, China. *Mar. Pet. Geol.* **2025**, *176*, 107346. [CrossRef]
47. Du, X.; Jin, Z.; Zeng, L.; Liu, G.; He, W.; Ostadhassan, M.; Song, Y.; Liang, X.; Yang, S.; Lu, G. Formation of natural fractures and their impact on shale oil accumulation in the Mahu Sag, Junggar Basin, NW China. *Int. J. Coal Geol.* **2023**, *279*, 104385. [CrossRef]
48. Wang, S.; Wang, G.-W.; Wang, H.-Z.; Liu, M.-J.; Huang, L.-L.; Huang, Y.-Y.; Wang, Z.-S.; Li, S.-Q. Logging evaluation of acoustic anisotropy and its relationship with "sweet spots" in lacustrine shale oil reservoirs: The Fengcheng Formation of the Mahu Sag, China. *Pet. Sci.* **2025**, *22*, 3133–3151. [CrossRef]
49. Zhi, D.; Tang, Y.; He, W.; Guo, X.; Zheng, M.; Huang, L. Orderly coexistence and accumulation models of conventional and unconventional hydrocarbons in Lower Permian Fengcheng Formation, Mahu sag, Junggar Basin. *Pet. Explor. Dev.* **2021**, *48*, 43–59. [CrossRef]
50. Seewald, J.S. Organic–inorganic interactions in petroleum-producing sedimentary basins. *Nature* **2003**, *426*, 327–333. [CrossRef]
51. Lewan, M.D. Experiments on the role of water in petroleum formation. *Geochim. Cosmochim. Acta* **1997**, *61*, 3691–3723. [CrossRef]

Disclaimer/Publisher's Note: The statements, opinions and data contained in all publications are solely those of the individual author(s) and contributor(s) and not of MDPI and/or the editor(s). MDPI and/or the editor(s) disclaim responsibility for any injury to people or property resulting from any ideas, methods, instructions or products referred to in the content.